CONTINUUM AND LINE EMISSION IN CYGNUS A

ALAN STOCKTON[1,2] AND SUSAN E. RIDGWAY[2]
Institute for Astronomy, University of Hawaii, 2680 Woodlawn Drive, Honolulu, Hawaii 96822
SIMON J. LILLY[2]
Department of Astronomy, University of Toronto, Toronto, Ontario M5S 1A7
Received 1993 December 30; revised 1994 March 17

ABSTRACT

We present the results from (1) imaging observations of Cygnus A in five essentially line-free continuum bands with central wavelengths ranging from 0.34 to 2.1 μm, (2) imaging observations in five narrowband filters centered on the emission lines Hβ, [O III] λ5007, Hα, [N II] λ6583, and [S II] $\lambda\lambda$6716,6731, and (3) deep spectroscopy covering the entire central region of Cyg A. We confirm that the featureless spectrum component is to be identified with the prominent double morphology at the center of Cyg A, but uncertainties in the distribution of the dust in this region tend to limit the accuracy with which we can determine its morphology and spectral-energy distribution (SED). From regions that appear to be least affected by obscuration, we find $f_\nu \sim \nu^{-0.1}$ for this component. This SED could be consistent with free–free emission, a population of young stars, or a quasar continuum scattered by electrons, but probably not with a quasar continuum scattered by dust, which would be bluer. Our spectroscopy places an upper limit on the equivalent width of broad Hβ that is well below that of typical quasars, showing that this flat-spectrum component (FSC) is almost certainly *not* dominated by scattered quasar radiation. Appeals to scattering by hot electrons to smear the scattered broad lines into invisibility appear to fail because the large density scale height of the electrons and the inefficiency of electron scattering should result in smoother and more extensive structure than we observe. Although the relative SED is consistent with free–free emission, the required amount of hot gas violates other observational constraints. At high angular resolution, the apparent morphology of the FSC is spiral-like. Although this impression may be partly due to obscuration, the distribution of the dust itself only serves to reinforce the spiral-like nature of the material with which it is associated. We conclude that the FSC is most likely radiation from a starburst at the center of Cyg A. Fits to the radial surface-brightness profile of the late-type component after our best efforts at removing the FSC allow us to estimate the wavelength dependence of extinction in the central region. A comparison with simple models for sources embedded in dust indicates that ~50% of the emergent blue flux from the late-type stars at the center may be due to scattered radiation. This large scattered contribution (which probably applies as well to the FSC and the emission-line component), together with a modest asymmetry in the radiation field, could plausibly account for the observed polarization properties of the inner region of Cyg A. Systematic differences are present between the distribution of [O III] on the one hand and [N II] (and other low-ionization species) on the other. After a large common component to the distribution is removed, the remaining [O III] excess is aligned with the radio axis, while the [N II] excess is distributed in what appears to be a planar structure perpendicular to the radio axis. The association of dust with this latter component indicates that it is a distinct morphological structure and not simply the result of shadowing effects. The emission-line intensities in the high-ionization regions are consistent with photoionization by a power-law continuum; those in the low-ionization region are similar to those seen in LINERs and appear to be consistent with ratios expected from x-ray photoionization. We find a systemic redshift for Cyg A of 0.05562 ± 0.00015, from a measurement of the strongly diluted Mg I b feature in high-S/N spectra of the central region. The velocity field of the ionized gas is quite complex, showing at least two components along the line of sight in many regions. In general, discrete clouds show velocity curves consistent with rotation rather than with outflow, but high-velocity gas, probably associated with the radio jets, is seen on both sides of the galaxy nucleus. The ionized gas centered on the nucleus is counter-rotating relative to the bright cloud to the NW and most of the fainter material in the same area. We conclude that, while there are strong reasons for believing that Cyg A harbors a hidden quasar (the presence of a point x-ray source,

[1]Department of Physics, University of Durham, South Road, Durham, DH1 3LE, England.
[2]Visiting Astronomer, Canada–France–Hawaii Telescope, operated by the National Research Council of Canada, the Centre National de la Recherche Scientifique of France, and the University of Hawaii.

 0004-6256/94/108(2)/414/23/$0.90

evidence from the emission lines of a flat photoionizing continuum, and the probable recent detection of scattered broad Mg II), there is no evidence that a significant amount of quasar optical or IR continuum has been scattered into our line of sight. Although the optical continuum peaks are roughly aligned with the radio structure, it is unlikely that there is any physical correspondence with the alignment between continuum and radio structure seen in luminous radio galaxies at high redshifts. Finally, the counter-rotating gas in the nuclear region, the secondary IR peak 1″ N of the nucleus, the evidence for star formation in the nuclear mini-spiral, and the extensive ragged swath of low-ionization gas and dust stretching to the NE and S all suggest that Cyg A has suffered a recent merger.

1. INTRODUCTION

Observations over the past several years of previously unsuspected phenomena in powerful radio galaxies at high redshifts (e.g., Chambers *et al.* 1987; McCarthy *et al.* 1987) encourage a detailed reexamination of the one radio galaxy of similar power in our own neighborhood, Cygnus A, at $z=0.056$. Remarkably, Cyg A remains the most powerful radio galaxy in the 3C catalog out to $z\sim1$. The most striking feature of optical images of Cyg A is the double morphology seen in the inner few arcseconds of the galaxy. Baade & Minkowski (1954) saw this double structure as two galaxies in collision; more recent work has viewed Cyg A as a single galaxy, interpreting the double structure either as the consequence of a bifurcating dust lane (Osterbrock 1983) or as some sort of asymmetrically distributed emission (Pierce & Stockton 1986). Van den Bergh (1976) showed that the western component was dominated by emission lines, while the eastern component was dominated by continuum radiation: the apparent near equality of the components in many broadband images results from a fortuitous balance of emission lines and continuum in most of the standard filters. Osterbrock (1983) found that a featureless-spectrum component dominates the continuum radiation over the central few arcsec, strongly diluting the late-type stellar absorption lines from the underlying elliptical galaxy. Pierce & Stockton (1986) identified this spectral component with the double morphology, which is therefore in some sense *excess* radiation, and not simply a normal nuclear bulge with a dust lane [Thompson (1984) had already surmised this on purely morphological grounds]. Pierce and Stockton suggested that the radiation may have been scattered from a hidden central nucleus, an interpretation that fits in well with recent attempts to unify quasars and radio galaxies (e.g., Barthel 1989). Such radiation should be polarized, and at least three polarization studies have been carried out to test this hypothesis. These studies have been hampered by the low galactic latitude of Cyg A (6°) and resulting uncertainties in the galactic foreground contribution to the polarization, but it is apparent that the intrinsic polarization in Cyg A in the optical is $\lesssim2\%$ (Goodrich & Miller 1989); however, imaging polarimetry by Tadhunter *et al.* (1990) showed that the polarization position-angle map agrees well with that expected for scattering from a central source. Both the continuum radiation and the narrow emission lines are polarized (Goodrich & Miller 1989; Jackson & Tadhunter 1993), but, at least in the blue, the continuum shows significantly greater polarization (Jackson & Tadhunter 1993). In other recent work, Djorgovski *et al.* (1991) detect a peak at the position of the compact radio source in images at K and L' and suggest that this is the quasar nucleus, and Vestergaard & Barthel (1993) have emphasized the importance of patchy extinction in the inner regions of Cyg A.

After the original submission of this paper, we received two important preprints of papers dealing with topics closely related to our own results. Antonucci *et al.* (1994) have detected broad Mg II λ2798, apparently scattered from a hidden quasar nucleus; and Tadhunter *et al.* (1994) have carried out a detailed analysis of spectroscopy of the ionized gas for two slit positions in Cyg A. We have included brief discussions of these results at appropriate points.

The observations we describe here are directed towards attempting to better understand the nature of the featureless continuum component, the physical mechanisms underlying the distribution, ionization structure, and velocity field of the gas, and the role extinction effects play in mediating our view of these components. Our imaging data have been obtained in six broad continuum bands centered from 0.34 to 2.1 μm, as well as in five narrow bands centered on emission lines. We also discuss spectroscopy covering essentially all regions showing significant line emission.

2. OBSERVATIONS

2.1 Images

Our core set of imaging observations (three line-free continuum filters, four emission-line filters) were obtained with a focal reducer and the IfA/Galileo TI 500×500 CCD system at the Cassegrain focus of the Canada–France–Hawaii Telescope (CFHT). We subsequently extended the spectral range of our continuum images by observations at the University of Hawaii 2.2 m telescope at 3400 Å with a TI 800×800 CCD and at K' with a NICMOS3 256×256 IR camera. We obtained additional images with HRCam at the CFHT prime focus, using a SAIC 1024×1024 CCD. Finally, we have included and reanalyzed the Hα–[N II] image discussed by Pierce & Stockton (1986). Table 1 gives a summary of all of our imaging observations. As indicated there, we will refer to our five optical continuum bands, having Cyg A rest-frame central wavelengths of 3217, 4263, 5629, 5781, and 7125 Å, as, respectively, u, b, v, v', and r. The initial reduction followed standard techniques appropriate to each of the instruments. Dome flats were used in all cases except for the HRCam observations, where twilight flats were used instead.

Most of our final CCD images were obtained by median averaging the individual frames, but we have used the IRAF/STSDAS implementation (ACOADD) of the Lucy–Hook deconvolution/coaddition algorithm (Hook & Lucy 1992) to

TABLE 1. Imaging observations.

UT Date	Filter			Exposure	Scale	Seeing	Telescope/Detector
	λ_C (Å)	FWHM (Å)	Band	(s)	(px^{-1})	(FWHM)[a]	
1983 Aug 5	6951	100	Hα/[N II]	1500	0.″30	0.″78	CFHT/TI 500 × 500 CCD
1986 Jul 2	6960	20	[N II]	6 × 600	0.″30	0.″94	CFHT/TI 500 × 500 CCD
1986 Jul 3	4506	352	*b*	8 × 300	0.″30	0.″85	CFHT/TI 500 × 500 CCD
1986 Jul 3	5950	500	*v*	20 × 60	0.″30	0.″87	CFHT/TI 500 × 500 CCD
1986 Jul 3	7531	361	*r*	10 × 120	0.″30	0.″81	CFHT/TI 500 × 500 CCD
1986 Jul 3	5145	74	Hβ	5 × 900	0.″30	0.″92	CFHT/TI 500 × 500 CCD
1986 Jul 4	7105	80	[S II]	4 × 600	0.″30	0.″85	CFHT/TI 500 × 500 CCD
1986 Jul 4	5300	28	[O III]	2 × 1200	0.″30	1.″06	CFHT/TI 500 × 500 CCD
1989 Oct 28	3402	276	*u*	4 × 1800	0.″14	0.″85	UH/TI 800 × 800 CCD
1989 Oct 29	3402	276	*u*	4 × 1800	0.″14	0.″85	UH/TI 800 × 800 CCD
1990 Aug 12	5293	27	[O III]	3600	0.″13	0.″69	CFHT/SAIC 1000 × 1000 CCD
1990 Aug 12	6965	28	[N II]	3600	0.″13	0.″73	CFHT/SAIC 1000 × 1000 CCD
1990 Aug 12	6110	1240	*v*′	10 × 300	0.″13	0.″71	CFHT/SAIC 1000 × 1000 CCD
1990 Oct 28	21100	3500	*K*′	25 × 70	0.″37	0.″74	UH/NICMOS3 256 × 256 IR

[a]Value given is that measured from the combined images, except for the *v*′ and *K*′ bands, for which the images were combined using *acoadd*. For these cases, the median seeing for the series is given.

combine our 10 continuum frames obtained with HRCam and our 25 *K*′ frames. The FWHM of the seeing profile ranged from 0.″59 to 0.″85, with a median of 0.″71, for the continuum HRCam images, and from 0.″67 to 1.″04, with a median of 0.″74, for the *K*′ images. We have carried the deconvolutions to 330 and 140 accelerated iterations, respectively; in each case we convolved the result with a Gaussian profile having a FWHM equivalent to that of the PSF of the best of individual image in the series. This procedure allows efficient combining of the data, retaining the resolution of the best frames without introducing significant artifacts. We have also carried out Lucy–Richardson deconvolutions of our single [O III] and [N II] frames obtained with HRCam (see Sec. *4.3.2*).

Because all of our CCD bandpasses were nonstandard and were defined by interference filters with roughly square transmission profiles, we used the spectrophotometric standard stars BD+17°4708 and Wolf 1346 (Oke & Gunn 1983; Massey *et al.* 1988) and mean extinction corrections for calibration of the images. The filter response curves were convolved with the spectral energy distributions of the standards to obtain standard flux densities for each of the passbands, from which system responses were then determined. The *K*′ data have been calibrated from observations of the *K* standard HD 203856, corrected for the nonstandard bandpass according to the prescriptions of Wainscoat & Cowie (1992).

We have attempted to correct these calibrations for relative systematic errors by smoothing them, using stars in the Cyg A field. We use the baseline given by our *u* and *K*′ measurements to compare the average of three of the bluer stars in the field with stars in the Gunn & Stryker (1983) spectrophotometric atlas that also have measurements at *K*. The G8 III star θ^1 Tau and the K0 III stars HD 124679 and HD 131111 not only fit the gross $U-K'$ color, but generally match the photometry in the other filters as well. In our correction procedure, we make a slight linear adjustment to the mean spectrum of the three Gunn–Stryker stars so that it exactly matches the *u* and *K*′ photometry of the average of our three field stars. We then scale the photometry for the remaining bands to match the stellar spectra. The mean root squared correction was 8%, and the largest correction was 18%.

Our basic calibration procedure leaves our data in units of erg cm^{-2} s^{-1} Å^{-1}. For our emission-line bands, after we have subtracted the continuum, we want these in units of total line flux (erg cm^{-2} s^{-1}), so we can determine line ratios. In order to make this conversion, we multiply the flux density by the effective width of each of the relevant filters, which we define as the width of a rectangular profile having the same integral as the actual filter profile and a transmission equal to the filter's transmission at the observed wavelength of the line.

We have converted all of the images to a common scale and alignment by means of the IRAF tasks GEOMAP and REGISTER, using ten stars surrounding Cyg A that were present and unsaturated on most of the images and confining the mapping to linear scaling and rotation. The rms deviation of these linear fits was better than 0.″015. For each of the line images, appropriate linear combinations of the two relevant bracketing continuum images were scaled to remove the stellar envelope and any other continuum components.

2.2 Spectroscopy

All of the spectroscopy we will discuss here was obtained at the CFHT on 1991 Sep. 2 and 3 UT with the Institute for Astronomy Faint-Object Spectrograph and a thinned Tektronix 1024×1024 CCD. Image slicers giving either three contiguous slits 1.″4 wide or three slits 0.″7 wide on 1.″4 centers were used for all observations, allowing essentially complete coverage, with considerable overlap, of the extended emission region. Slit positions are indicated in Fig. 1. The spectra covered the range from Hβ to the [S II] λλ6716,6731 doublet. Offsets were made from the bright star 21″ E of the center of Cyg A. Although the slit placement was less consistently precise than we had hoped it would be, we obtained

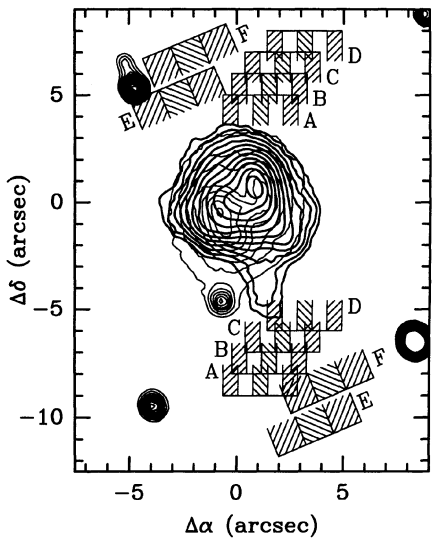

FIG. 1. Image-slicer slit coverage of Cyg A. Heavy contours are of the [N II] image, light contours are of the v image. The origin is centered on the IR nucleus. Slit positions and coverage are indicated by the connection of shaded portions of corresponding brackets: slit groups A–D have 0.″7 slits on 1.″4 centers; E and F have contiguous 1.″4 slits. The actual slit lengths were 49″ and in every case extended well beyond the borders of this diagram. For this plot and all following images, N is at the top and E to the left.

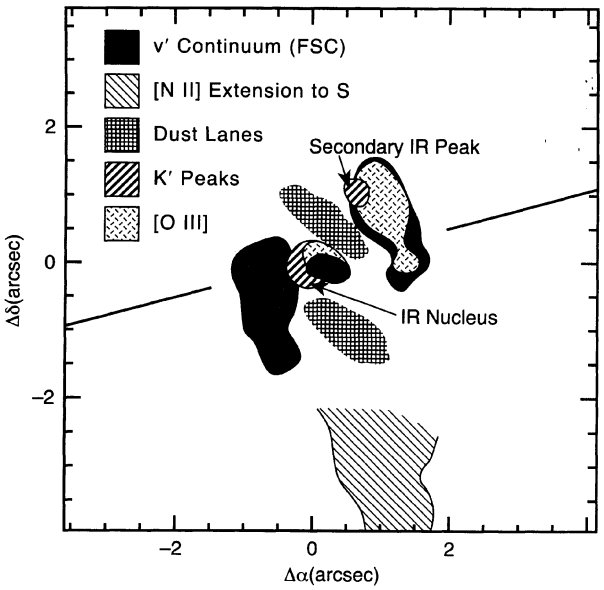

FIG. 3. Schematic diagram showing major morphological components in the inner region of Cyg A. The coordinates are centered on the IR nucleus. The diagonal line indicates the radio axis.

images of the field and of the slit through the spectrograph before (and usually after) all of our spectroscopic exposures, and we can therefore locate our actual slit positions relative to features in Cyg A to an accuracy of ~0.″1. The maximum drift seen over the course of our exposures (all of which were 3600 s), as indicated by our field images before and after, was 0.″18.

After standard bias subtraction and flatfielding of the CCD frames, the individual two-dimensional spectra for each of the three image-slicer slits were extracted from each frame. Sky-background subtraction and wavelength calibration were carried out using standard IRAF tasks. Small zero-point adjustments were made in the wavelength scale to correct the night-sky lines to their proper rest wavelengths. A spectrophotometric calibration, based on observations of the standard G191B2B, was applied, although the effect of atmospheric refraction and the narrow slits used in many of our observations mean that even *relative* fluxes of lines at the extreme ends of our spectral range may be in error by as much as 20%.

We are concerned almost exclusively with the emission lines, and, for most of our analysis here, we have zeroed the continuum individually for each row of our (multispec-format) spectra. We have attempted to deredden the spectra, assuming a standard galactic reddening law. We first removed an estimated $E(B-V)=0.4$ (Kronberg *et al.* 1977; Spinrad & Stauffer 1982; Yee & Oke 1978) of galactic foreground reddening; then, using a redshifted (but otherwise standard) extinction curve, we adjusted the $H\alpha/H\beta$ ratio to 3.0, close to the expected Case B value (see Sec. *4.3.2*). Note that this procedure assumes that the extinction of the emission-line clouds can be approximated by a simple screen, which is almost certainly not strictly true; fortunately, most of the line ratio comparisons we will be making span only small wavelength regions and are therefore insensitive to modest errors in our calibration and reddening corrections. To first order, this procedure will also correct for any errors in our relative spectrophotometric calibration.

3. A FIRST LOOK AT THE IMAGES

Figure 2 (Plate 10) shows the central 21″ square region of Cygnus A for each of our continuum and line bandpasses (except the HRCam images, which essentially duplicate bandpasses represented in Fig. 2). The continuum images show the decreasing relative importance of the double continuum structure as one moves from shorter to longer wavelengths. New features emerge in the K' image. There is a luminosity peak (Djorgovski *et al.* 1991) lying between the positions of the optical double components and, within the errors, coincident with both the center of the elliptical envelope isophotes and the compact radio source. We will refer to this component as "the nucleus" for convenience, but in doing so we do not mean to prejudge its nature. A secondary peak is visible ~1″ N and slightly W of the nucleus (the scale at Cyg A is almost exactly 1″ kpc^{-1} for $H_0=75$ km s^{-1} Mpc^{-1}, which we adopt, so one can essentially interchange arcsec and kpc here and elsewhere in this paper). We discuss these and other continuum structures seen at K' in Sec. *4.1*. Since it is sometimes difficult to visualize from the individual images the relative spatial relationships of components seen in different bands, the major ones we shall be discussing are shown in schematic form in Fig. 3 (the details of some of the components shown are dependent on material presented in later sections of this paper). We also indicate the position angle of the radio axis.

It is clear that there is a complex interplay among the various continuum components and extinction effects in the central regions of Cyg A. We attempt to sort these out, at least at a rudimentary level, in Sec. *4.2*, where we also estimate the SED of blue double continuum structure.

All of the emission-line images show the same basic pattern: a main peak coincident with the NW optical continuum peak, a second peak at the position of the IR nucleus, and an extended distribution of weaker emission. However, as we discuss in Sec. *4.3.1*, there are important differences in detail that point to physically distinct components to the extended emission. We examine the detailed structure of the inner region in Sec. *4.3.2*, using deconvolutions of the two emission-line images and one continuum image we obtained with HRCam. We also attempt to interpret how what we see might be modified by variable extinction across the emission-line region by examining the Hα/Hβ ratio map to infer the distribution of reddening, which should correlate with at least the foreground component of the extinction. We compare the positions of the central peak at different wavelengths in Sec. *4.4*. The contributions of the various continuum and line components to the total observed flux in specified apertures are summarized in Sec. *4.5*. We discuss details of our spectra in Sec. 5. In Sec. *5.1*, we examine limits on the presence of scattered broad-line radiation; in Sec. *5.2*, we discuss the velocity field of the emission-line gas; and in Sec. *5.3*, we use dereddened line ratios to look at variations in ionization conditions in the emission-line region. Finally, in Sec. 6, we bring the results of this investigation together with previous work in discussing the nature of the featureless continuum component, the implications of the observed velocity field of the ionized gas, the relation of Cyg A to powerful radio galaxies at high redshift, and what Cyg A has to contribute to the question of unification of radio galaxies and quasars. We summarize our results in terms of a schematic model of the inner regions of Cyg A in Sec. 7, where we also mention a few directions for future work.

4. DISTRIBUTIONS OF CONTINUUM AND LINE COMPONENTS

4.1 Surface-Brightness Profile and Morphology at K′

Among our images, both extinction and the featureless-continuum component should be minimized at K', so we consider this image first.

Some emission lines lie within our K' bandpass (principally Pa-α and Si VI λ1.962 μm), so we need to consider to what extent such emission will influence our judgement of the continuum morphology. Spectrophotometric measurements (Ward *et al.* 1991) indicate that the emission-line flux in the K' bandpass over a 5″ centered aperture accounts for ~6% of the total, and free–free and free–bound emission will contribute ~2% more. Since we find the nearly point-like nuclear component to contain ~8.5% of the K' flux over this aperture (Sec. *4.5*), it is possible, as Vestergaard & Barthel (1993) have suggested, that this nucleus is almost purely emission-line radiation—but only if the nucleus were to contain essentially *all* of the emission-line flux. Our Hα/Hβ ratio map (see Sec. *4.3.2*) indicates no more reddening at the nuclear position than at the peak of the line emission (coincident with the NW continuum peak): both have Hα/Hβ=4.5 ±0.5 (in excess of galactic foreground reddening), implying $A_V \sim 1.4 \pm 0.35$ if the reddening were all to be due to dust between us and the source, and if the extinction were to follow a standard reddening law. From the Pa-α/Hβ ratio, Ward *et al.* (1991) obtain $A_V = 1.2 \pm 0.15$ for the emission-weighted average over a 5″ aperture, in excellent agreement with the value of 1.35±0.3 previously determined by Lilly & Hill (1987). The agreement of the values for extinction based on Hα and Pa-α indicates that most of the screen-like component of the extinction is distributed, rather than strongly concentrated around the emission-line clouds, and that optical depth effects are not large. This result, taken together with the near-equality of the extinction in the optical at the two principal emission-line peaks, indicates that their intensity ratio in the K' band should not be very different from what it is in the optical. We therefore believe the K' nucleus to comprise mostly continuum radiation, a conclusion that is reinforced by the fact that, in Sec. *4.3.2*, we clearly resolve the central emission-line component into an elongated structure, whereas (as we describe below) the K' nucleus is barely resolved and remains round.

Because the nucleus is strong only in the K' image and tends to obscure more subtle structure in the inner region, we remove it before comparing the K' image with our other continuum images. While Djorgovski *et al.* (1991) refer to the nucleus they see at K and L' as "unresolved," we find that a point-source model appears to undersubtract the wings relative to the center. Convolving a Gaussian with a FWHM of 0.″3±0.″1 with our PSF gives the cleanest subtraction, although there is of course some latitude in the choice of scaling. We have chosen the one that removes as much luminosity as possible without producing a positive gradient anywhere in the radial surface brightness profile. Such profiles, with and without the nucleus, are shown in Fig. 4; they have been calculated by fitting a simple elliptical isophote model (fixed ellipticity 0.228 and fixed PA −13.°8) to the respective images, ignoring regions with foreground stars or other discrete components. However, they still include the effects of any extinction. The ellipse center giving the best fit to the envelope lies 0.″17 SW of the nucleus; given possible errors in flatfielding and field variations in galactic extinction, this offset is probably consistent with 0. We obtain a fairly good fit to a de Vaucouleurs $r^{1/4}$ law over the range $1.''5 < a \lesssim 20''$; over the more restricted range from $3.''5 < a < 12''$, where we are most confident of the quality of our profile, we find $r_e = 65'' \pm 10''$, in reasonable agreement with previously obtained values of 74″ (Pierce & Stockton 1986) and 59″ (Carilli *et al.* 1989). The flux in the nucleus we have removed corresponds to $m_{K'} = 16.4$ (prior to any correction for galactic extinction), in good agreement with Djorgovski *et al.* (1991), who find $m_K = 16.2 \pm 0.5$. If we are correct in our impression that the nucleus is resolved with a FWHM of ~0.″3 (~300 pc), then we are not seeing the presumed quasar nucleus directly, but instead, most likely, hot dust in the nuclear region [Antonucci (1993) has also suggested this possibility because of the lack of detection of broad lines at 2 μm by Ward *et al.* (1991); however, with the nucleus comprising less than 10% of the flux in their 5″

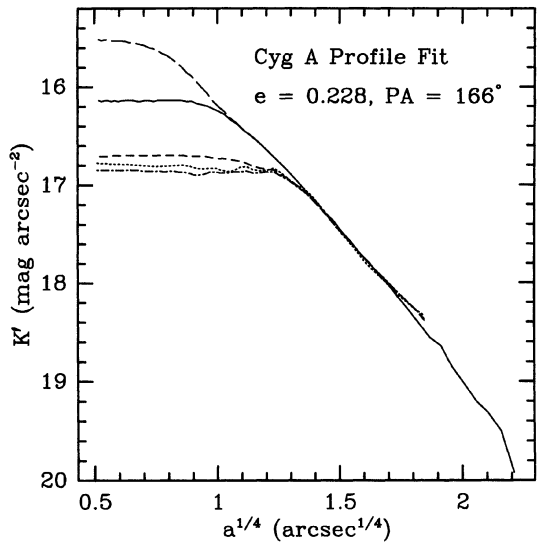

FIG. 4. Elliptical surface brightness profiles. *Long dashed curve: K′* image with nucleus; *solid curve: K′* image without nucleus. *Lower three curves:* Profiles from other continuum images, after removal of the FSC as described in the text, scaled to match *K′* profile in outer envelope. Short dashed curve, *r* image; dotted curve, *b* image; dot–dashed curve, *v* image. For all curves, obvious discrete objects have been ignored, including asymmetric structure near the nucleus.

aperture, it is not clear that the lack of detectible broad lines in the spectrum of Ward *et al.* is a strong constraint]. With no additional reddening along the line of sight, the photometry of Djorgovski *et al.* (1991) at *K* and *L′* gives a lower limit to the dust temperature of ~500 K. Any significant reddening would increase this value.

Finally, we can subtract the elliptical isophote model from the original *K′* image to emphasize nonelliptically symmetric structure. Figure 5(e) and its inset show the residual images without and with the nucleus, respectively. Note that the secondary peak to the N of the nucleus, while very red, now appears to be part of an elongated diffuse feature that could be be related to the NW component of the double morphology seen in the optical. A fainter feature, corresponding to the SE optical component, is also present; these features differ from their optical counterparts in that their contrast is lower and separation smaller.

4.2 Featureless Continuum and Extinction in the Central Region

The normal stellar absorption features in the central region of Cyg A are strongly diluted by the blue "featureless continuum" component that Osterbrock (1983) estimates accounts for about 60% of the light at 5000 Å (anticipating our result below, we will henceforth refer to this as the "flat-spectrum component," or "FSC"; in contrast, we will designate the radiation from the late-type stars as the "elliptical component"). Pierce & Stockton (1986) showed that this FSC had to come from a resolved source, which they identified as the two peaks in the optical continuum surface brightness that lie close to the center of the galaxy. This identification of the FSC with the principal morphological peculiarity of Cyg A means that the latter cannot be fully explained by appealing to a dust lane crossing the nucleus of an otherwise normal elliptical galaxy (e.g., Osterbrock 1983). The double structure in the inner regions must be at least partly due to an addition of luminosity to the underlying elliptical stellar distribution, rather than simply subtraction of luminosity from it.

What is the origin of this excess luminous component? Pierce & Stockton (1986) suggested that the FSC was analogous to a galactic bipolar nebula and resulted from continuum radiation scattered from a central source hidden from our direct view; they therefore expected it to show significant polarization. Goodrich & Miller (1989), however, found that the net intrinsic integrated optical continuum polarization in the central region of Cyg A was less than 1% and consistent with 0%; they argued, by process of elimination, that the FSC was simply a population of hot stars. Subsequent imaging polarimetry by Tadhunter *et al.* (1990) showed that the polarization, though peaking at only ~2% in their *V* bandpass, did, in fact, show the position-angle distribution expected for light scattered from a central source. Goodrich & Miller (1989) had found that both the continuum radiation and the emission lines were polarized; they assumed that the emission lines would have no intrinsic polarization and attributed the polarization of both components to foreground interstellar polarization in our own galaxy. Jackson & Tadhunter (1993), however, have used spectropolarimetry of another galaxy close to Cyg A to determine the galactic component of polarization in this region: they find a polarization of ~0.5% at a position angle nearly perpendicular to that found for both continuum and emission lines in Cyg A. Since Jackson & Tadhunter also find significant polarization in the emission lines, they attribute this component to interstellar polarization in Cyg A. The additional polarization in the continuum, which amounts to about 1% at 5000 Å but is close to 0% near Hα, they consider to be scattered radiation from a hidden central nucleus. However, they also place fairly stringent upper limits to the presence of broad Balmer lines in the polarized spectrum and conclude that there is no evidence at present that the nucleus is a quasar.

In order to investigate the situation further, we have attempted to disentangle the various continuum components present in the inner regions of Cyg A. Our first approach was to scale the model fit to the envelope of the *K′* image (Sec. *4.1*) to the envelope of each of the optical continuum images (normalizing to a region whose outer limit was defined by an ellipse of constant surface brightness with a semimajor axis of 6″ at PA 170°; the inner limit was irregularly shaped to avoid the FSC and a foreground star). The scaled models were then subtracted from the corresponding images. This approach assumes that intrinsic differential radial color gradients are not significant, and that the elliptical symmetry of the relaxed stellar component is undisturbed by irregular extinction. We have evidence from the difference images (i.e., the *u*, *b*, *v*, *r*, and *K′* images, minus the appropriately scaled *K′* model), shown in Fig. 5 (Plate 11), that this latter assumption, at least, is not strictly true: there is an apparent bisymmetric pattern of extinction, stronger to the north of the

nucleus, affecting at least the elliptical component. That the extinction is most obvious in our v and r bands is due to the diminishing dominance, in the b and u bands, of the elliptical component, which contributes much of the total central surface brightness at the longer wavelengths. In the u band, the elliptical component is virtually invisible.

Figure 5(f) is a version of the sum of the v and r difference images [Figs. 5(c) and 5(d)], at high contrast and with the lookup table inverted to emphasize weak negative features. It shows that, in addition to the region of strong extinction near the center of Cyg A, a faint finger of dust extends about 5″ to the south.

It is clear from Fig. 5 that we are unlikely to achieve a unique decomposition of the inner morphology of Cyg A from our data, because we cannot independently determine both the profile of the underlying elliptical component (as modified by extinction) and the distribution of the FSC. The best we can hope to do is to arrive at a plausible decomposition based on simplified models; this approach may give us a reasonable qualitative view of the situation, but any quantitative results must be taken with some caution.

Guided by the apparent distribution of reddening seen in Fig. 5 and the apparent strength of the FSC in our b and u images, we make the working assumption that at least some parts of the FSC are not significantly reddened by dust within Cyg A itself. If we can isolate the FSC in one image, we can scale and subtract it from the other continuum images, looking for a smooth residual across the boundary between the elliptical component and the bluest regions of the FSC, which are least likely to have suffered significant reddening. We are depending here on the fact that the FSC has quite sharp boundaries, and we are implicitly assuming that extinction of the elliptical component does *not* produce a similarly sharp discontinuity in the same region. Once we have determined scalings that, when subtracted, leave the smoothest residuals for the various calibrated continuum images, the scaling factors themselves then give a relative SED for the FSC. The cleanest example of the FSC is potentially our u image with the scaled K' model subtracted (because the late-type stellar component is extremely weak at this wavelength, the amplitude of any variation in it due to extinction is even less significant). One worry is the effect of Balmer continuum emission. We estimate from our Hβ image that the Balmer continuum contributes $\lesssim$20% of the FSC flux, most of which will be in the NW peak. We concentrate on the bluest part of the FSC, which is *not* the NW peak but the region to the S of it, roughly due W from the nucleus, where the Balmer continuum emission should be small.

This u image also suffers from relatively low signal-to-noise, so we use a version of it that has been median smoothed over a 0.″65×0.″65 box. The uncertainties in the SED were estimated by noting the range in scaling at which the characteristic FSC pattern was just discernable as either a positive or negative image.

The SED we obtain is shown in Fig. 6, along with the SED for the elliptical (derived from an elliptical annulus from which regions covered by the FSC, emission lines, and foreground stars have been deleted). The flat spectrum shown by the FSC appears to support our assumption that at least some regions of it have low intervening reddening (within Cyg A) along our line of sight. Shown also for reference are typical E/S0, Im, and quasar continuum SEDs, as well as the free–free continuum from a 10^6 K plasma. It is clear that the FSC SED that we have determined is consistent with the Im, quasar, or free–free continuum, particularly since even a small amount of uncorrected extinction between us and the FSC could differentially depress the u point. We will discuss all of these possibilities in detail in Sec. *6.1*. Given that the FSC components are fairly closely aligned with the radio axis, it is of interest that the aligned components of powerful radio galaxies at high redshifts appear to have similarly flat SEDs (Rigler *et al.* 1992). We shall take up the matter of similarities and differences between such galaxies and Cyg A in Sec. *6.4*.

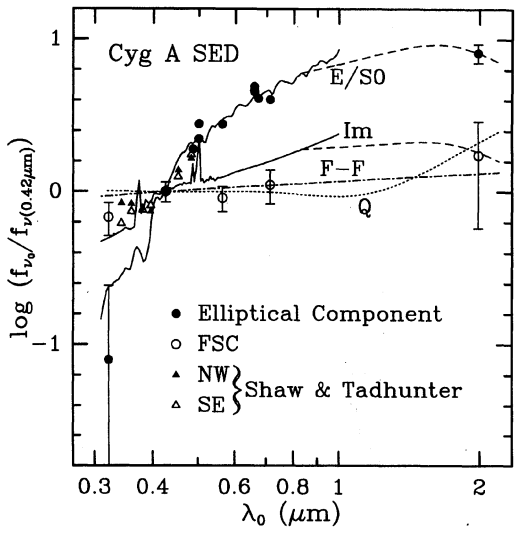

FIG. 6. Spectral-energy distributions of the flat-spectrum and elliptical components of Cyg A. Unless specifically shown, typical error bars are like that shown on the normalization point at 4200 Å. SEDs for the Coleman *et al.* (1980) E/S0 and Im models, extended by *IJHK* photometry, are shown for comparison, as are the average quasar continuum of Sanders *et al.* (1990) and free–free emission from a 10^6 K plasma. Filled and open triangles are based on data of Shaw & Tadhunter (1994) (see text for details).

Shaw & Tadhunter (1994) have recently attempted to determine the SED of the FSC by a technique of spectral decomposition. In the same way our morphological decomposition approach is dependent on assumptions regarding the *smoothness* of the underlying elliptical component, their approach depends on assumptions regarding the *color* of the elliptical component and particularly variations in reddening. They have used emission-line ratios to estimate the reddening, but considerable uncertainty remains both because the effective depth of the different components in the dust distribution may differ and because the proper reddening law to use for interpolating or extrapolating from the emission-line wavelengths depends not only on the properties of the dust grains, but on the relative geometry of the sources and the dust. We have plotted on Fig. 6 Shaw and Tadhunter's SEDs for the NW and SE peaks, assuming that the colors of the elliptical component have been reddened by standard extinction with E($B-V$)=0.4 over their assumed galactic extinc-

tion of $E(B-V)=0.36$. These have been derived from their Figs. 7(a) and 7(b); however, for comparison with our SED, we have removed their correction for the assumed reddening of the FSC itself. The slopes of the SEDs determined by the two methods agree well at the shorter wavelengths, but theirs is redder than ours near 5000 Å. At these longer wavelengths, systematic errors in the determination of the underlying elliptical component will tend to dominate over random errors, since the FSC is becoming a progressively smaller portion of the total measured signal (the approach taken by Shaw and Tadhunter assumes that the FSC component is negligible at ~8600 Å).

Our procedure of scaling our shortest wavelength image to edge effects in the bluest regions of the FSC clearly *undersubtracts* any parts of the FSC that are significantly reddened. In order to obtain a somewhat better removal of the FSC, leading to a more accurate model of the elliptical component (as modified by internal extinction), we split the FSC model derived from the u image into three parts, which are then scaled independently. Because we are still scaling to a smoothness criterion dependent on edge gradients, we are presumably still undersubtracting in regions where reddening is important; but this procedure does give us sufficient freedom to accomplish a first-order removal of the FSC in our b, v, and r bands. We then fit elliptical isophotes to the residuals, using the same fixed center, ellipticity, and position angle as for the K' fit in Sec. *4.1*. We iterate this procedure, using our derived b surface-brightness model (instead of the K' model) to scale and subtract from our u image to construct our FSC templates.

A comparison of the elliptical surface-brightness profiles, scaled at large semimajor axis values to the K' profile, is shown in Fig. 4. Note that the b, v, and r profiles show very little difference in shape from each other and are almost flat out to 2".5. While we again caution that the numerical details of this exercise in decomposition are perhaps unreliable, we emphasize that our smoothness criterion should, if anything, work to *minimize* any change in slope in each of the profiles.

But isn't the fact that the b, v, and r profiles show significant extinction, but little or no reddening, sufficient reason for doubting the accuracy of the profiles? Not necessarily: in fact, the behavior shown in Fig. 4 (i.e., a substantial difference between the K band and visual extinction, but little difference in extinction among the b, v, and r bands) appears to be a general feature of certain classes of models incorporating dust embedded in stellar distributions (Witt *et al.* 1992). Two factors are working to reduce reddening at visible wavelengths: transmitted stellar radiation is weighted in favor of stars with little extinction (and thus little reddening), and the reddening that *is* present is at least partly compensated by a blue contribution from scattered light. These effects are shown in Fig. 7, where we compare our normalized extinctions from Fig. 4 to the simplest model given by Witt *et al.* (1992): a uniform spherical distribution of sources embedded in a coextensive uniform distribution of dust. Although this particular distribution is unrealistic as a model, it demonstrates the general features that a more realistic model would also be likely to show: note, especially, that in the blue, fully half of the light comes from the scattered component. While the details will clearly depend on the exact geometry of the relative distributions of stars (and other sources) and dust, a common feature of models that can reproduce the qualitative colors we see is that a significant fraction (≳30%) of the emergent flux in the mid-optical region is from scattered, rather than direct, radiation.

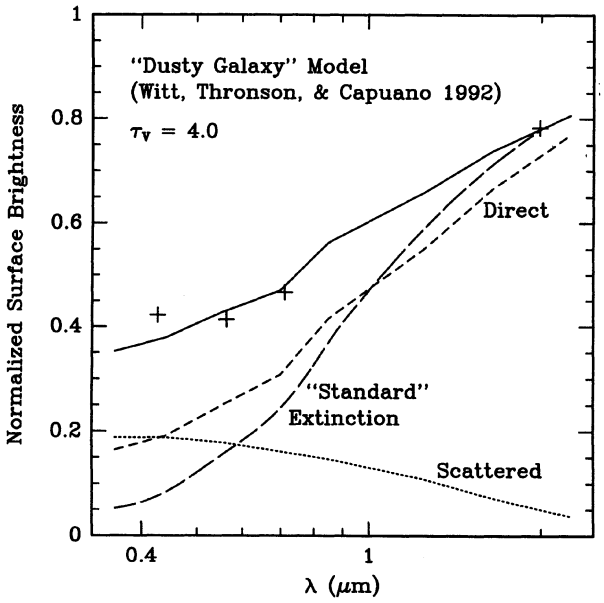

FIG. 7. Extinction of the elliptical component in the central region of Cyg A (crosses), fitted to the "dusty galaxy" model of Witt *et al.* (1992) with $\tau_V=4$. This model is simply a sphere in which sources and dust are both uniformly distributed, such that the optical depth in the V band to the center of the distribution is 4. Contributions from the direct and scattered components are shown, and all curves are normalized to the SED of the sources if no dust were present. A "standard extinction" curve, normalized to the K' point, is also shown for comparison.

We can now subtract models constructed from these profiles from the original images to obtain an approximation of the FSC alone at each wavelength (this procedure is not completely circular because the median averaging of pixels in each ellipse annulus of the model profile minimizes the effect of the structure left behind by our crude FSC-subtraction procedure). The accuracy of these representations will depend on how smooth and symmetric the actual distribution of extinction is, and the residual FSC images are still subject to any variable extinction across the FSC itself. The FSC images are shown in the upper-right inserts in the appropriate panels of Fig. 5.

We shall look more closely at the inner continuum morphology in Sec. *4.3.2*, but first we examine the gross properties of the extended emission.

4.3 Extended Line Emission

4.3.1 Relative distributions

We have mentioned that the emission-line images in Fig. 2 all show the same general features present in the Hα–[N II] image of Pierce & Stockton (1986): the main peak in the luminosity distribution is close to the NW continuum peak,

and the secondary peak near the position of the IR nucleus. However, even a cursory look at the line images shown in Fig. 2 reveals at least one significant difference between the distribution of [O III] λ5007 emission and that of all of the other lines: the [O III] does not show the extensions to the S and NE present for the rest (seen best in the [N II] image). Because of the wide range in surface brightness covered by these line images, it is difficult to get a good feeling for differences in the relative line intensity distributions by comparing images or even series of images at different contrasts. Instead, in Figs. 8(a)–8(d) (Plate 12), we show the result of scaling our [O III] and [N II] images to each other and subtracting; such a difference map emphasizes differences in the distributions of the higher-surface-brightness regions. A similar qualitative appearance is shown by the line-ratio map shown in Fig. 8(e), which weights high- and low-surface-brightness regions equally. The [O III] emission (and, presumably, that of other high-ionization lines) predominates in two regions aligned along the radio axis, while the excess [N II] emission tends to lie in an irregular swath roughly perpendicular to this direction.

We showed in Sec. *4.2* how, by subtracting a model based on our K' image from our optical images, we are able to trace, in the sum of our v and r images, a faint extension of dust in projection against the elliptical envelope out to ~5″ S of the nucleus [Fig. 5(f)]. It now appears that this dust correlates with the extension of the low-ionization gas in the same direction. This correlation suggests two things: first, that the low-ionization component to the S (and, by implication, the weaker extension to the N) reflects the actual distribution of the gas and is not, say, simply the result of illumination effects; and, second, that the association of significant amounts of dust with the low-ionization component may serve to constrain interpretations of its origin.

4.3.2 The distribution of ionized gas and extinction in the central region

We have not specifically singled out our HRCam images up to now, although the HRCam [O III] and [N II] images were the basis for the discussion of large-scale differences between the distributions of these species in Sec. *4.3.1* and Fig. 8. Although the seeing on the night on which we obtained these images was variable and never better than ~0.″6, these images have both the best seeing and the best image scale of any in our dataset.

While it is unfortunate in most respects that Cyg A is at such low galactic latitude, at least one compensation is that we have good PSF reference stars at small angular distances from Cyg A. We have already mentioned (Sec. *2.1*) that the ten v' continuum frames were combined using the Lucy–Hook deconvolution/coaddition procedure. We have also deconvolved our single continuum-subtracted [O III] and [N II] images, using ACOADD with 300 accelerated iterations for each. Because the high surface brightness of the emission in the central few arcseconds results in quite high signal-to-noise, we can retain good resolution in our restoration of these images with hardly any problems from artifacts of the deconvolution process. Conversely, the lower surface brightness in the continuum limits our ability to push the resolution of our v' image.

Our results are shown in Fig. 9 (Plate 13). Figure 9(a) shows the original [O III] image, with a seeing FWHM of 0.″69; Fig. 9(b) shows the deconvolved image, restored with a Gaussian to a FWHM of 0.″30; and Fig. 9(c) shows for comparison a similarly restored version of our other [O III] image, obtained with a focal reducer. We do not expect this last image to respond as well as the HRCam image to deconvolution: the focal reducer produces some field variation in the PSF, the seeing for this image, at 1.″06, was the worst of any of our images, and the original pixel scale of 0.″3 is over twice as coarse as that of the HRCam images. The restoration clearly is worse, as expected; nevertheless, the basic structure seen in the two images agrees quite well. This comparison gives us considerable confidence in the details seen in our restored HRCam image.

Figures 9(d)–9(f) shows the corresponding set of [N II] images. Here the original HRCam image FWHM was 0.″71, the original focal-reducer image FWHM was 0.″94, and the HRCam image has once again been restored to a FWHM of 0.″30. The same general structure is seen as in [O III], although there are differences in the relative intensities of some components, and the [N II] distribution is more diffuse. The relative distributions are seen more clearly in Fig. 9(g), which shows the difference between [N II] and the [O III] images.

Figure 9(h) shows the v' image, with a restored FWHM of 0.″55, only slightly smaller than that of the best individual frame in the series.

As is evident from Fig. 3, the gap or minimum in the [O III] emission to the NW coincides with the radio jet and may result from evacuation of this region by it. The peculiar, semiring-like structure to the SE may be similarly associated with the jet on that side. One additional result of these higher-resolution studies is the impression that the morphologies of the FSC and the emission-line region are actually *more* similar than they appear at lower resolutions. In both cases there is a basic spiral-like structure; this tends to get washed out at lower resolutions, and the apparent morphology is dominated by the relative brightness differences of the various components, which differ strongly between continuum and emission-line images. We will discuss the morphology in detail in Sec. *6.1.2*: here it is sufficient to note that the images appear to show linear dust features to the NW and SE of the central peak. These same features also can be seen in our model-subtracted K' image [Fig. 5(e)].

Reddening in the emission-line region can be determined from variations in the hydrogen-line ratios, but there are at least three potential problems with using these ratios to infer the extinction.

First, as we have already mentioned in another context (Sec. *4.2*), the interpretation of reddening as a measure of extinction is complicated if the dust is mixed with the emitting gas. Some degree of intermixture seems likely.

Second, narrow-line regions photoionized by AGN continua typically show some enhancement of Hα and Lyα over standard Case B predictions because of collisional enhancement of the lower levels in the large, partially ionized zone produced by high-energy photons (e.g., Gaskell & Ferland 1984; Ferland & Osterbrock 1985). Empirical ratios for

Hα/Hβ~3.1 are found for AGN with apparently unobscured narrow-line regions, instead of the standard Case B value of 2.85 (for $T_e = 10^4$ K); however, in Cyg A, extinction probably weights the narrow lines in favor of the lower-density parts of the transition region, and we will assume an intrinsic ratio of 3.0, although the difference between this value and 3.1 is of no importance for our results.

Finally, as a practical matter, our present dataset does not include an Hα image *per se*: we have to derive one from our calibrated Hα+[N II] and [N II] images. Because [N II] λ6583 is typically stronger than Hα by a factor of ~1.5, this procedure depends critically on the accuracy of our calibration and our knowledge of our filter transmissions. It is very difficult to estimate the likely magnitude of these systematic uncertainties, but they do mean that our numerical results should be viewed with some degree of caution. We will be emphasizing the general distribution more than the exact numbers in any case.

The integrated Balmer decrement for Cyg A observed by Osterbrock & Miller (1975) clearly indicated local extinction of the emission-line region, once it had become clear that the extinction could not be galactic (Kronberg *et al.* 1977), and this result has been confirmed from the Paα/Hβ ratio (Lilly & Hill 1987; Ward *et al.* 1991), which is immune to collisional effects because both lines come from the same upper level. Pierce & Stockton (1986) found substantial spatial variations in the Hα/Hβ ratio across the emission-line region.

Figure 9(i) shows a greyscale representation of the Hα/Hβ line ratio, after correction for an assumed galactic $E(B-V)=0.4$. We have masked off regions where noise is likely to dominate the ratio by excluding pixels for which either Hα or Hβ fell below appropriate limits. The ratios in the region shown range from ~2.0 to ~8.0; both of these extremes lie near the edge of our masked region and are likely affected by systematic uncertainties in one or both of the line images. The elongated region of high reddening to the SE of the IR nucleus correlates well with one of the dust "lanes" seen in the optical continuum images. The other, to the NW of the nucleus, which is the more apparent in the optical images, also seems to have a counterpart (though a less definite one) in the ratio image. It is probably this lane that Tadhunter *et al.* (1994) are seeing when they note a maximum in the Hα/Hβ ratio between the FSC peaks. In regions where the ratio image can be expected to be fairly trustworthy, the largest reddening is seen about 0.″5 S of the nucleus and in the tail-like structure 2″ W and 1″ S.

4.4 The Positions of the Central Peaks

All of the deconvolved HRCam images show a peak near the center, as of course does the K' image. We have measured the positions of these peaks to an absolute precision of about 0.″2, using positions of stars close to Cyg A given by Griffin (1993). Vestergaard & Barthel (1993) quote a private communication from Carilli and Perley giving the position of the compact radio core as $19^h57^m44^s.43$, $+40°35'46''.37 \pm 0''.1$ (1950). For the position of the IR nucleus, we find $19^h57^m44^s.46$, $+40°35'46''.30 \pm 0''.2$ (1950); and for the central peak in our HRCam v' image, we find $19^h57^m44^s.43$, $+40°35'46''.11 \pm 0''.2$ (1950). Although both of these positions are within the stated errors of that of the radio core, they are definitely not coincident with each other. We shall assume that it is the IR peak that is coincident with the radio core. From a direct measurement on our registered images, we obtain an offset of the HRCam v' peak from the IR peak of $\Delta\alpha = -0''.30 \pm 0''.03$ and $\Delta\delta = -0.06 \pm 0.03$. Similar measurements of the [O III] and [N II] central peaks with respect to the IR peak give, respectively, $\Delta\alpha = -0''.22 \pm 0''.02$ and $\Delta\delta = 0.11 \pm 0.02$ and $\Delta\alpha = -0''.08 \pm 0''.03$ and $\Delta\delta = 0.13 \pm 0.04$.

4.5 Contributions from Continuum and Line Components to the Observed Flux

Table 2 gives flux density contributions for the elliptical component, the FSC, and the nucleus, and total fluxes in the emission lines for four regions near the center of Cyg A. Estimated errors due to calibration uncertainties are 10%–20%, but the relative contributions of the FSC and the elliptical component are subject to additional unknown systematic uncertainties, as described in Sec. 4.2. The data given in this table are observed values, prior to any correction for galactic extinction; note also that the passband central wavelengths given in the second column are in the observed frame.

These estimates of the contributions from the various continuum and emission-line components can be useful in evaluating broadband observations that include both continuum and emission lines. For example, we can attempt to correct the polarization amplitude obtained by Tadhunter *et al.* (1990) for dilution effects in the V band. We consider first the case where the stellar background and emission lines do not contribute to the observed polarization. We take the flux densities for the FSC and the elliptical component in our v filter (5650 Å) as being effectively the same as the average over the standard V filter. We then approximate the V band fluxes by multiplying by the effective width of the V filter, which we take to be 900 Å. Almost all of the emission-line flux in the V band is due to [O III] emission: we simply take our measured [O III] λ5007 flux in the same aperture and multiply it by 1.34 to account for [O III] λ4959. At the SE continuum peak, 0.″7 E and 0.″3 S of the IR nucleus, we find that the surface brightness (in units of erg s^{-1} cm^{-2} arcsec^{-2}) in the V band due to emission lines is 1.74×10^{-14}, that due to the elliptical component is 1.4×10^{-14}, and that due to the FSC is 9.7×10^{-15}; the fractional contribution of the FSC is then ~0.24. This means that the polarization of ~2% in the V band found by Tadhunter *et al.* (1990) would give a polarization of ~8.5% for the FSC.

However, this value is critically dependent on the assumption that neither of the presumed diluting components is itself polarized. We have no information on the polarization of the elliptical stellar component in the inner regions, but both Goodrich & Miller (1989) and Jackson & Tadhunter (1993) have found that the emission lines show some polarization. If we take the value of the continuum polarization near [O III]

TABLE 2. Photometry of continuum and emission-line components.

			Flux Density[a] or *Flux*[b]			
		Position:	IR Nucleus		SE Peak	NW Peak
		Δα, Δδ:	0″.0, 0″.0		0″.7, −0″.3	−1″.0, 0″.9
Band	λ_C (Å)	Aper. Diam:	5″	1″.5	1″.5	1″.5
u	3402		6.7/1.2	0.96/0.12	1.21/0.11	0.96/0.11
b	4506		9.2/11.8	1.38/1.09	1.79/1.11	1.22/1.10
Hβ	5145		*11.2*	*1.96*	*1.53*	*2.52*
[O III]	5293		*144.2*	*27.0*	*22.9*	*34.9*
v	5950		8.8/29.6	1.39/2.67	1.90/2.75	0.91/2.75
Hα	6951		*60.8*	*12.2*	*7.9*	*16.7*
[N II]	6965		*96.3*	*19.0*	*13.2*	*24.2*
[S II]	7105		*16.8*	*3.61*	*2.26*	*4.21*
r	7531		9.0/38.1	1.39/3.95	1.77/3.86	1.38/3.70
K′	21100		3.0/19.1	1.07/2.40	0.75/2.19	0.49/2.00
K′	21100		1.9/19.1[c]	0.21/2.40[c]	0.34/2.19[c]	0.42/2.00[c]

[a]For the continuum bands, flux densities are given for the FSC (including any other components not included in our elliptical models) and for the elliptical component as F_{FSC}/F_{ELL}. The units are 10^{-17} erg cm^{-2} s^{-1} Å^{-1}. The errors are dominated by systematic calibration uncertainties, estimated to be 10—20%, and by the uncertain separation of the FSC from the elliptical component (see text).

[b]Emission-line fluxes are given in *italics* and are in units of 10^{-15} erg cm^{-2} s^{-1}. Errors are typically ~10%.

[c]These values are for the *K′* image with the nucleus subtracted as described in the text.

of 2.32% given by Jackson & Tadhunter (1993) and interpolate the FSC fraction from our *b* and *v* bands, we obtain an FSC polarization of ~4.6%, again assuming that the elliptical component is unpolarized. We will discuss the probable validity of this assumption in Sec. *6.1.1*.

We will use our measurements of the fractional contribution of the FSC to the continuum flux density at *b* and *v* to estimate the fraction at Hβ in Sec. *5.1*, where we discuss upper limits to the presence of scattered broad lines.

5. LINE PROFILES, LINE RATIOS, AND VELOCITY FIELD OF THE IONIZED GAS

5.1 Scattered Broad Lines?

If the FSC were primarily due to scattered radiation from a hidden central source, and if this source is a quasar nucleus, then we should see scattered broad-line radiation, as is seen, for example, in polarized light in the narrow-line radio galaxy 3C 234 (Antonucci & Barvainis 1990). Jackson & Tadhunter (1993) have searched unsuccessfully for evidence for broad lines in the polarized component. But the FSC in Cyg A is so strong that, if it were dominated by scattered quasar radiation, one should be able to see scattered broad lines in high-quality spectra even in unpolarized light. We do see a broad wing on the blueward side of the narrow-line Hα–[N II] group for slit positions just NW of the nucleus. However, we are convinced that this feature, first noticed by Tadhunter (1991), is not evidence for the broad line we seek. First, it is present only near the weaker FSC peak and is clearly not observed in the stronger; second, our upper limits on a corresponding feature at Hβ imply a considerably steeper Balmer decrement for the broad-line region than is usually seen in quasars; and third, the feature occurs only at positions where we see the high-velocity gas (Tadhunter 1991). This last is the most telling argument, since Hα in the high-velocity component would fall exactly where we see the excess flux, and it could easily blend with the wing of the narrow [N II] λ6548 line to give the result we see [Fig. 10(a)]. By scaling the [O III] λ5007 profile in the high-velocity system to the best fit to the observed wing and assuming Case B (with the reddening correction determined for the strong lines), we can estimate what we should see at Hβ. Figure 10(b) shows that there appears to be a feature with the expected strength at the expected position.

The equivalent widths of the Balmer lines in quasars are remarkably constant from object to object (Yee 1980). Because of the presence of the strong [N II] lines bracketing Hα, we get our best limit on the presence of scattered broad lines from the equivalent width of Hβ in our spectroscopy of the SE peak of the FSC, where the FSC has its highest surface brightness and the narrow-line emission is relatively weak (Fig. 11). From our photometry given in Sec. *4.5*, we estimate that the FSC accounts for ~50% of the continuum at the position of the SE peak at Hβ. Using this fraction of the observed continuum as our assumed scattered quasar continuum, we superpose plots of typical broad-line profiles having FWHM and equivalent widths equal to the minimum and the median of these quantities in seven low-redshift steep-spectrum quasars observed by Baldwin (1975). We estimate that, for lines with FWHM ~50 Å, we can set an upper limit to the broad Hβ equivalent width (again, relative to our best estimate of the FSC alone) of 15 Å, or about one-third that of the weakest broad Hβ line in Baldwin's sample.

5.2 Velocity Field

We have fitted Gaussian components to the [O III] λ5007 line and the Hα–[N II] λλ6548,6583 group for each row in which any of them are detected in each of our 18 slit posi-

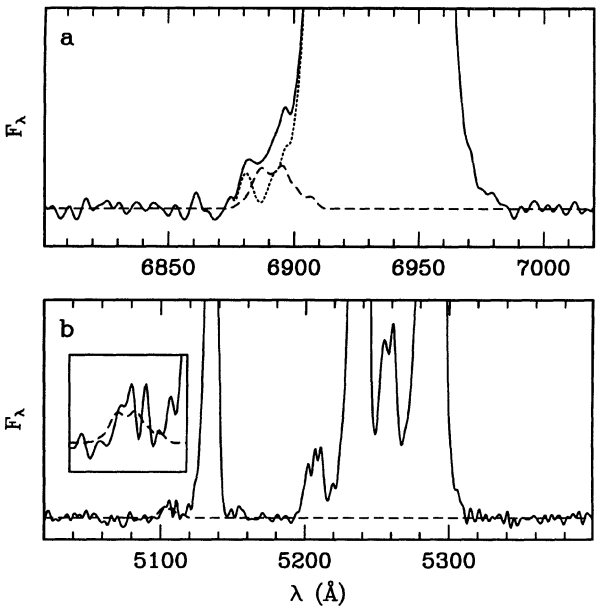

FIG. 10. Sum of two spectra covering the emission-line peak NW of the nucleus. (a) Hα region, showing wing on blueward side of the [N II] λ6548 line. The dashed curve shows fit of a scaled high-velocity-system [O III] λ5007 line at the expected position of Hα in this system, and the dotted line is the residual after removing this component. (b) Similar display of the Hβ region, where the high-velocity profile from (a) has been scaled by a further factor of 0.35 (the Case B ratio) and shifted to the expected position of Hβ in the high-velocity system. The inset shows an enlargement of the high-velocity Hβ region.

tions. Where only one velocity system is present, single Gaussians fit the profiles quite accurately, occasionally missing a small amount of flux in the wings. The decompositions of profiles where there are two velocity systems look equally good, and in no case was it necessary to resort to more than two components in deconvolving a blend.

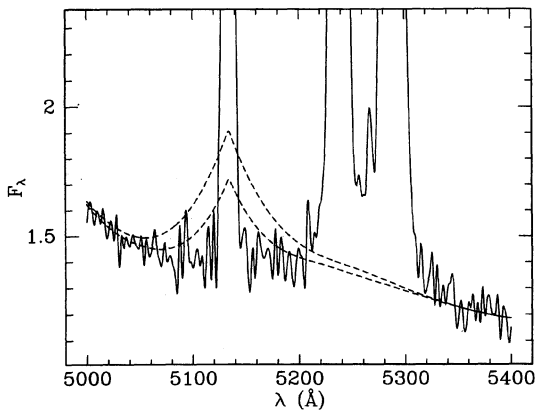

FIG. 11. Region near Hβ in the sum of two spectra centered on the SE continuum peak. The slit width is 1".4; regions ±1".3 along the slit on each side of the continuum peak have been summed. F_λ is in units of 10^{-16} erg cm^{-2} s^{-1} Å^{-1} and has been corrected for standard galactic extinction assuming E($B-V$)=0.4. The dashed curves show schematic broad Hβ profiles having FWHM of 40 and 55 Å, and equivalent widths of 45 and 103 Å, respectively. See text.

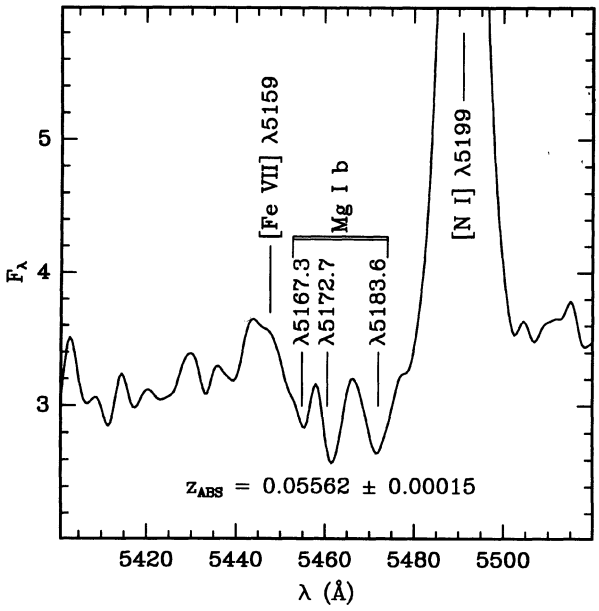

FIG. 12. Sum of four spectra crossing the nuclear region, showing the Mg I b feature. The peak between λ5167 and λ5172 is largely due to a weak, but poorly subtracted, night-sky line.

We wish to plot radial-velocity curves relative to the systemic velocity of Cyg A, but how do we estimate this systemic velocity? The well known weakness of the absorption-line spectrum in the center of Cyg A (Osterbrock 1983) has meant that most of the radial velocities given in the literature are based on the emission lines themselves, and the irregular distribution of ionized gas does not encourage us to believe that any sort of average emission-line velocity will be a very trustworthy measure. From a position 5" N of the nuclear region, Spinrad & Stauffer (1982) give an absorption-line redshift $z=0.0567\pm0.0016$, but this value is not very precise and may be biased by its off-center location. Four of our spectra using wide slits essentially straddle the position of the IR nucleus, and we have summed these together over a centered effective aperture of 6"×3". The result in the region of the Mg I b feature is shown in Fig. 12. The three components Mg I λλ5167,5173,5184 are seen nestled between the [Fe VII] λ5159 and the [N I] λ5199 lines, although the profiles of the two shorter wavelength components are distorted by the weak residual of a night-sky line lying between them. We base our redshift on the λ5184 component, from which we obtain a heliocentric redshift of $z=0.05562\pm0.00015$. Using this redshift as our zeropoint, we plot in Figs. 13(a)–13(d) the radial velocity curves for [O III] λ5007 and [N II] λ6583 for each of our slit positions.

These plots need some explanation. The center of each square gives the position (Δy) of a row in the spectrum relative to that of the IR nucleus in the dimension parallel to the slit and the velocity (ΔV_r) of that component relative to the systemic velocity determined from the Mg I b feature. Each vertical pair of panels is at a different slit offset Δx from the IR nucleus, measured from the centerline of the slit. If the slit PA=0°, Δx is positive towards the E and Δy is

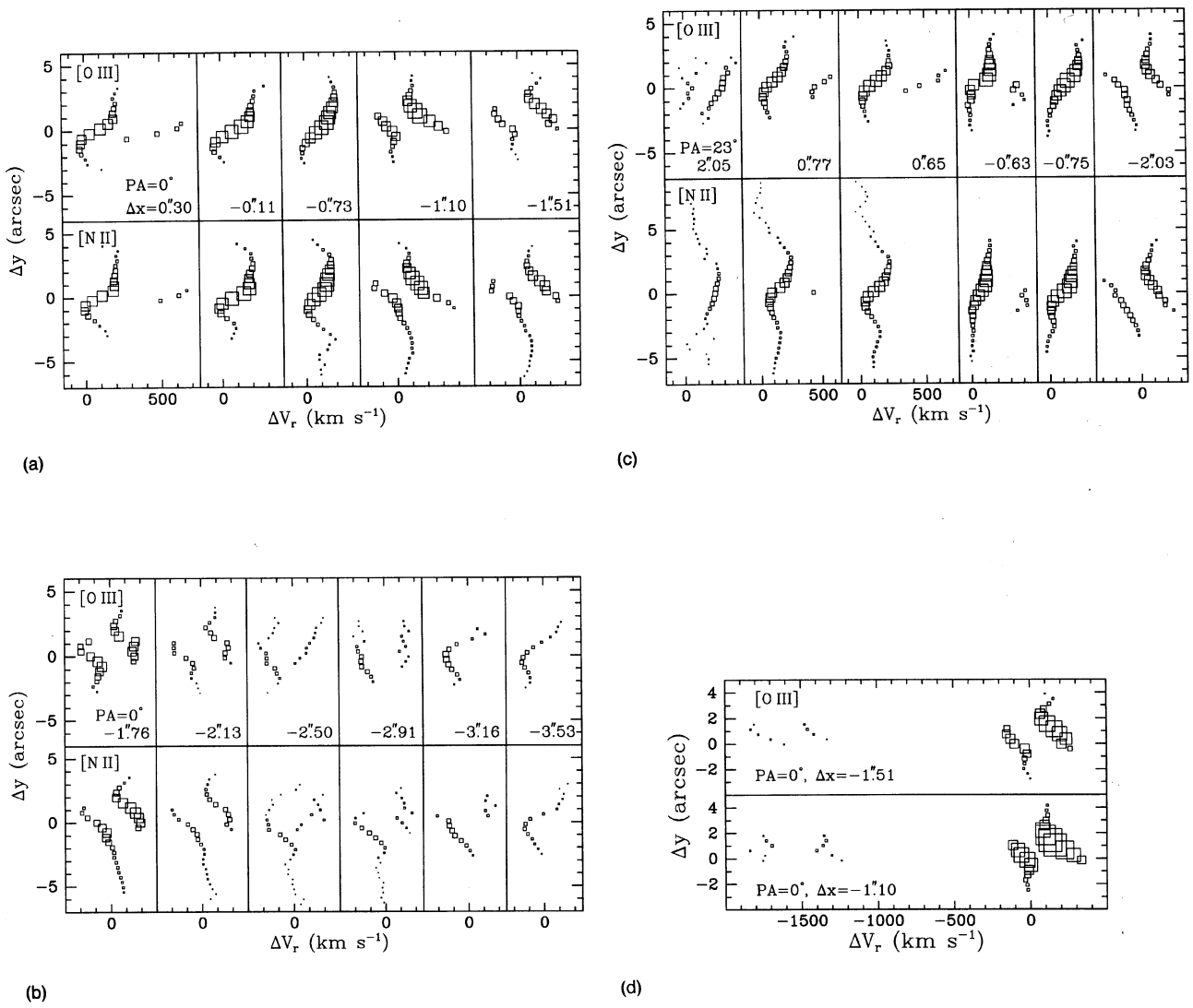

FIG. 13. Radial velocity curves for [O III] λ5007 and [N II] λ6583 for all slit positions for which emission is detected. Offsets Δx and Δy are in arcsec from the IR nucleus in the slit coordinate system, where the x axis is perpendicular to the slit and the y axis parallel to it. See text for details. (a) and (b) Slit positions at PA=0°, with 0.″7 slit widths. (c) Slit positions at PA=23°, with 1.″4 slit widths. (d) Repeat of the 4th and 5th [O III] panels from (a), with high-velocity components included.

positive towards the N. Within each individual panel, the area of the square is proportional to the intensity of the component at that point, but this proportionality is only roughly maintained at different slit positions, and [O III] and [N II] have different scalings for display purposes.

Because of the extension of the low-ionization component to the S and NE, the [N II] curves often cover a larger range along the slit than do the [O III] curves. One limitation of this procedure that must be kept in mind in interpreting these velocity curves is that seeing blur will affect the measured velocities where there is a large gradient in intensity: e.g., consider a gas cloud in solid-body rotation and of uniform surface brightness aligned along the slit: seeing effects at the ends of the cloud will produce an artificial flattening of the rotation curve at these points. A second limitation is that, with intensity, wavelength, and σ as free parameters, there were cases where it was not clear whether fitting with one or two components was more appropriate. We generally took the position that, if we could get a reasonably adequate fit with a single component, we would use that fit and go to two components only if forced to do so. In so doing, we may in a few cases not have recognized real double-valued velocities. We also have usually ignored second components if they were less than 10% of the intensity of the primary unless the velocity separation was such that they were obviously real. Nevertheless, there are likely some situations where an asymmetric profile actually due to a continuous range of velocities has been deconvolved into two discrete components. One obvious candidate for such an occurrence is the first [O III] panel in Fig. 13(c) (slit PA 23°, Δx=2.″05), where the corresponding [N II] curve is single valued.

The most striking feature of these velocity curves is the

abrupt change in the character of the curves $\sim 1''$ W of the IR nucleus: the gradient of the velocity curve changes sign, and to the W of this divide there are two distinct components separated by ~ 300 km s^{-1}. We have created a two-dimensional [O III] image from the spectra by summing the [O III] profile for each slit position into a single column and replicating these on the projected slit positions on the sky, averaging in the regions where the slit areas overlap. This procedure was carried out separately for each of our two slit position angles. By comparing the resulting "images" with our actual narrowband filter [O III] images, we can confirm which morphological components our slits actually covered, including seeing effects. From this comparison, it is apparent that the change in the velocity field corresponds with the switch between spectra dominated by the emission-line component near the IR nucleus and those dominated by the more luminous component to the NW; i.e., velocities *increase* from S to N in the nuclear component but *decrease* from S to N in the NW component. Velocities also decrease from S to N in the secondary, lower-redshift component seen at slit positions $\gtrsim 1''$ W of the nucleus, which is clearly to be identified with the lower-surface-brightness material seen to the S and SW of the brightest emission-line component. This material also shows velocity continuity with the low-ionization component to the S.

A perhaps clearer view of the nature of the velocity field of the ionized gas in the inner region is given by Fig. 14 (Plate 14), which shows deconvolutions of images of the strong lines for the crucial slit positions. Progressing from top to bottom, we see for the slit position 0.″30 E of the nucleus mainly the linear velocity gradient of the nuclear component; to the N of the nucleus, the diffuse gas has velocities similar to those at the N end of the nuclear cloud, where, incidentally, we can also see evidence for some gas with a spread of velocities ranging upward. The spectra look generally similar at the $-0.''11$ slit position but change radically at the $-0.''73$ slit position: here we see clearly for the first time emission from the bright cloud to the NW, although we see only the NE, low-velocity end. At the same time, we have moved off the center of the nucleus and are recording emission only from its W edge. This image helps to clarify what is happening in the third pair of panels in Fig. 13(a): although the curve looks smooth, it is actually composite, with the southern, low-velocity end being dominated by the edge of the nuclear cloud and the northern, high-velocity end being due to the NE end of the bright NW cloud. At the $-1.''10$ slit position, we are firmly centered on the NW cloud and can see clearly that its velocity gradient is reversed from that of the nuclear cloud, as is that of the fainter gas to its S. The lines at $-1.''51$, where the slit has started to move off the peak of the NW cloud, look qualitatively similar.

Note that in the small region from about $1''$ to $1.''5$ W and $0''$ to $1''$ N of the nucleus there are actually four velocity components along the line of sight, including the high-velocity system first noticed by Tadhunter (1991) which we resolve into two components, with velocities of ~ -1400 and ~ -1750 km s^{-1} [these have been omitted from Fig. 13(a) but are shown in Fig. 13(d)]. The double-peaked profile of the high-velocity [O III] λ5007 line can be seen quite clearly in Fig. 10(b), and we see this double peak in both of our spectra covering the region where the high-velocity gas is visible. There is marginal evidence in our spectra that the two clouds responsible for these peaks cover slightly different spatial regions. We also see evidence for some weaker, lower-velocity peaks apparently associated with the same phenomenon. The high velocities and the position of these components in the direction of the W radio jet make it entirely plausible that they represent thermal gas entrained at the boundary of the radio jet.

Just to the E of the nucleus, there is a secondary component with positive velocities ranging up to ~ 600 km s^{-1}. This component may be associated with outflow on the E side, although no radio jet has yet been detected there.

TABLE 3. Relative line ratios in Cygnus A subcomponents.

Line	Nucleus	NW	S_1	S_2	S_3
Hβ λ4861	1.00±0.05	1.00±0.05	1.00±0.15	1.00±0.20	1.00±0.13
[O III] λ4959	3.50±0.18	3.28±0.16	0.57±0.15	0.67±0.19	0.67±0.13
[O III] λ5007	10.24±0.51	9.61±0.48	1.55±0.15	1.06±0.19	1.21±0.13
[N II] λ5200	0.46±0.02	0.28±0.03	0.32±0.14	0.64±0.18	0.44±0.12
[Fe VII] λ5721	0.05±0.02	0.04±0.02	<0.13	<0.18	<0.11
[N II] λ5755	0.10±0.02	0.08±0.02	0.10±0.12	0.15±0.16	0.11±0.11
He I λ5876	0.09±0.02	0.11±0.02	<0.15	<0.26	<0.16
[Fe VII] λ6087	0.07±0.02	0.05±0.02	<0.15	<0.19	<0.12
[O I] λ6300	0.80±0.04	0.75±0.04	0.87±0.09	1.09±0.12	0.73±0.08
[O I] λ6364	0.27±0.01	0.18±0.02	0.27±0.09	0.38±0.11	0.22±0.08
[Fe X] λ6375	0.01±0.02	0.01±0.03	<0.26	<0.25	<0.16
[N II] λ6548	1.78±0.09	1.94±0.10	1.74±0.09	1.60±0.10	1.65±0.08
Hα λ6563	3.00±0.15	3.00±0.15	3.00±0.15	3.00±0.15	3.00±0.15
[N II] λ6583	5.41±0.27	5.26±0.26	5.11±0.26	4.93±0.25	5.04±0.25
He I λ6678	0.04±0.02	0.04±0.02	0.06±0.06	0.19±0.08	0.08±0.06
[S II] λ6716	1.73±0.09	1.44±0.07	1.75±0.09	1.43±0.08	1.40±0.07
[S II] λ6731	1.46±0.07	1.25±0.06	1.21±0.06	1.24±0.08	1.18±0.06

5.3 Ionization Diagnostics

Even before there was any direct evidence for a source of nonthermal radiation in Cyg A, it was considered to be a classic example of photoionization by a power-law continuum (Baldwin *et al.* 1981; Osterbrock 1983). Such statements were based on line intensities averaged over much of the emission-line region. Because the line ratios show considerable variation over different regions, we look at the locus of different emission-line clouds in BPT-type plots (Baldwin *et al.* 1981; Veilleux & Osterbrock 1987).

We consider four regions: the nuclear emission-line cloud, the brightest peak (NW of the nucleus), the low-ionization extension to the S, and, to the extent possible, the high-velocity gas to the W of the nucleus. In each case, we have corrected the spectra to an Hα/Hβ ratio of 3.0 with a standard reddening law, first applied at zero redshift to correct for the assumed foreground galactic $(B-V)=0.4$, then applied at the redshift of Cyg A for the remaining correction. In order to enhance the detection of weak lines, we independently deredshift each row in our spectra before coadding to keep the summed linewidths as small as possible. Measured relative intensities of the emission lines for all components except for the high-velocity gas are given in Table 3, and line-ratio plots are shown in Fig. 15. Three independent spectra covering the southern low-ionization region were measured; these are designated S_1, S_2, and S_3 in the table

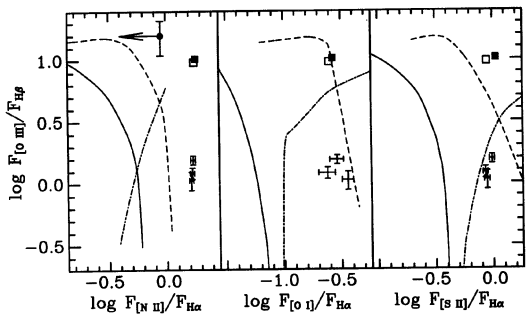

FIG. 15. Line-ratio diagrams for regions in Cyg A. The filled square and open square are for the nuclear peak and the NW peak, respectively; the error bars are smaller than the symbols. The filled circle showing an upper limit to the [N II]/Hα ratio is for the high-velocity gas NW of the nucleus. The three crossed error bars are from three independent spectra covering slightly different regions of the low-ionization extension to the south. Curves shown are from Veilleux & Osterbrock (1987): the solid curve is the empirical dividing line between H II region-like objects (to the left) and AGNs (to the right); the dashed curve is a solar-abundance power-law ionization model of Ferland & Netzer (1983), with the ionization parameter decreasing downwards and to the right; and the dot–dashed curve is a shock model of Shull & McKee (1979), with the shock velocity increasing upwards and to the right.

heading. Spectra of the bright NW component suffer confusion from a lower-velocity component over part of the slit coverage [see Fig. 13(a), $\Delta x = 1\farcs1$ slit position]. We have dealt with this overlap by carrying out Gaussian deblending of the profiles for each line of the spectrum in the overlap region and using the deblended line parameters to create an artificial two-dimensional spectrum of the lower-velocity component alone, then subtracting this image from the original spectrum, leaving only the higher-velocity component.

The errors given for the weaker lines in the table have been based on variances from Gaussian profile fits at random positions in each of the spectra, using a fixed Gaussian sigma characteristic of actual line fits. For the stronger lines, we take 5% of the line strength as a conservative estimate of the error in line flux and give that value whenever it is larger than the error estimate from the continuum noise.

Of special interest is the [Fe X] λ6375 line, which would indicate the presence of $\sim 10^6$ K gas. In the spectrum of the nuclear emission-line region there is definitely a feature near the expected position. But it lies on the wing of the [O I] λ6364 line, and, as Tadhunter *et al.* (1994) have noted, this identification is uncertain because other lines also show a component with a similar velocity separation. In fact, the feature seems clearly to be the redshifted component of [O I] λ6364 associated with the high-velocity system seen in the first pair of panels of Fig. 13. We have checked this supposition by doing a precise shift and scaling of the [O I] λ6300 line to the position and intensity of the [O I] λ6364 line, and subtracting. Whereas a direct measurement of the displaced component gives a significant intensity of 0.04±0.02 (relative to Hβ), the residual from the subtraction gives 0.01 ±0.02, which is the value we have given in Table 3. We therefore have no significant detection of [Fe X] at any position.

The ratios of the [S II] lines give $N_e \sim 300$ for the nuclear and NW peaks, as well as for two of the three measurements of the S extension. For the high-velocity gas, we have measurements only for the [O III] lines, Hα, and Hβ. We estimate an upper limit to [N II] λ6583 from [N II] λ6548 (since the former falls at essentially the same wavelength as the strong low-velocity [N II] λ6548). The locus of these measurements in Fig. 15 indicates that it is most likely that this gas is photoionized by the nuclear continuum source and that the ionization parameter is quite high. If this gas is at the same distance from the ionizing source as that in the NW peak, the density must be a factor of at least a few lower, indicating $N_e \lesssim 100$ cm^{-3}.

While some of the other lines show differences that are significant with respect to the formal errors, the only difference among the three remaining regions that is significant in an astrophysical sense is the relative strength of the [O III] lines between the nuclear and NW components on the one hand, and the S extension on the other (the other high-ionization lines are so weak that the upper limits on them in the S extension are of no interest). Even the low [O III] strengths seen in the S extension should probably be considered upper limits: the fact that no distinct corresponding feature is seen in our [O III] image leads us to believe that much of the [O III] emission that is present may be from a general, low-surface-brightness, high-ionization component on which the low-ionization structure is superposed. The relative constancy of the other line ratios is reflected in the nearly vertical separation of the points in the BPT diagrams in Fig. 15, which plot $\log F_{[O\ III]}/F_{H\beta}$ against $\log F_{[N\ II]}/F_{H\alpha}$, $\log F_{[O\ I]}/F_{H\alpha}$, and $\log F_{[S\ II]}/F_{H\alpha}$. The nuclear and NW components lie firmly within the power-law photoionized region of these diagrams. While the region in which the S extension points fall are also consistent with power-law photoionization, the situation is somewhat more ambiguous, since such ratios are found both in LINERs and in some emission-line regions associated with cooling flows. However, the high-ionization regions are almost certainly photoionized, and the consistency of the line ratios of low-ionization species among different regions suggests that photoionization is the dominant ionization mechanism in the S extension as well. The great relative strength of the [N II] lines in all components is clearly evident in the first panel of Fig. 15; Tadhunter *et al.* (1994) find that N/O must be enhanced by about a factor of 4 over the solar ratio.

The relatively strong [O I] emission indicates the presence of of a large, partially ionized zone, which implies that some of the gas is effectively shielded from radiation just beyond the Lyman limit. That is, along at least some sight lines to the photoionizing source, the fully ionized zone is radiation limited. At shorter wavelengths, where the absorption cross-section of H is sufficiently low, high-energy photons can penetrate to create the extended, partially ionized zone. This picture is consistent with the detection of an unresolved hard x-ray component along our line of sight (Koyama 1992), but no corresponding soft x-ray or UV component. The gas in the S extension presumably has a column density between it and the photoionizing source rather like the one along our line of sight. However, gas in the high ionization regions, which are preferentially aligned along the radio axis, must

see a much lower column density; the ionized regions may well be density limited along these sight lines.

6. DISCUSSION

6.1 The Origin of the Flat-Spectrum Component

The interpretation of the optical double structure at the center of Cyg A has been an important and contentious issue ever since Baade & Minkowski (1954) claimed it as evidence for colliding galaxies. The identification of this extended structure with Osterbrock's (1983) featureless spectrum component (Pierce & Stockton 1986) seems to leave only two realistic possibilities: either the source of the radiation is unresolved but hidden from direct view, and the apparent extension is due to scattering that takes place far from the source (Pierce & Stockton 1986), or the sources of the radiation are distributed more or less in the pattern we actually observe (Goodrich & Miller 1989), which presumably has been modified only by extinction. We consider these two possibilities from the standpoint of the various kinds of evidence now available.

6.1.1 Polarimetry

The principal evidence supporting the conjecture that the FSC is scattered radiation from a hidden central continuum source is the distribution of polarization position angles found by Tadhunter *et al.* (1990). If only the FSC were polarized, our analysis of the contributions of the various diluting components within the *V* band (Sec. *4.5*) indicates that the peak polarization of the FSC alone would be about 8.5%. However, the clear demonstration that the emission lines themselves show significant intrinsic polarization (Jackson & Tadhunter 1993) indicates both that the polarization of the FSC component must be $\lesssim 5\%$ and that understanding the polarization of the narrow lines may be important to our understanding of other polarized components in Cyg A. For the purposes of this discussion, we shall assume that Jackson & Tadhunter (1993) are correct in arguing that interstellar polarization in our own galaxy cannot account for the observed polarization in Cyg A.

First, we consider the possibility that a significant portion of the narrow-line radiation is itself hidden from our direct view and is scattered into our line of sight. Because the narrow-line gas is likely to be distributed over a region with a characteristic size $\gtrsim 1$ kpc, a much larger region of heavy extinction would be needed to hide it than is required to hide the central continuum source and broad-line region. Furthermore, while the apparent morphologies of the emission-line gas distribution and the FSC are similar, their intensity distributions are sufficiently different that it seems unlikely that they both reflect the distribution of scattering material. Thus, while we cannot eliminate this mechanism as a possibility, we regard it as implausible.

A second source of polarization for the emission lines could be aligned grains in Cyg A along our line of sight to the emitting gas. This is the mechanism favored by Jackson & Tadhunter (1993), and our Hα/Hβ map [Fig. 9(i)] supports there being a significant component of screen-like extinction in front of much of the emission-line gas. If the grains are coherently aligned over kiloparsec scales, some or all of the emission-line polarization may be due to such an interstellar polarizing screen.

However, there is a third possibility. Most of the dust that we detect in Cyg A is within a radius of 2″–3″ of the nucleus, i.e., the same region where we see the FSC and most of the emission-line material. We have circumstantial evidence (Sec. 4.2) that a large fraction of the emergent flux from the elliptical component in this region is *locally* scattered: might not this also be true for at least some of the emission-line radiation? And, given the strong spatial gradients we see in our emission-line images (e.g., Fig. 9), which will mean that many of the scatterers will see a strongly anisotropic radiation field, is it at all unlikely that such scattering should result in polarization at the levels observed ($\sim 1\%$)?

We have been discussing the emission-line radiation, because it is the polarization of this component that does not fit comfortably into the picture of polarization by scattering of a hidden central source and seems to require an additional polarization mechanism. But exactly the same argument applies to the FSC itself: its polarization, as well, could be due to scattering of radiation from embedded (or at least local) sources. For plausible initial SEDs, the FSC appears to be less reddened than the main peaks in the emission-line distribution, so it may have a higher proportion of scattered light. Its distribution, too, has rather sharp edges, implying anisotropic radiation fields and, hence, some degree of polarization of the scattered light.

Finally, it is not inconceivable that the elliptical component itself has a small intrinsic polarization from scattering. If we are correct in suggesting that a large fraction of its emergent flux from the inner region is scattered radiation, one only needs a suitable asymmetry in the radiation field. While such anisotropies are unlikely to be as large as for the emission lines or the FSC, they could be present as a result of local obscuration or even of the large-scale radial gradient in stellar density.

Note that this scattering from embedded sources would also tend to produce a polarization PA distribution qualitatively similar to one due to a central radiation source, but with lower polarization, because the anisotropy of the radiation field would be less extreme. Such models will depend strongly on the details of the geometry of the sources and scatterers, and it is beyond the scope of this paper to attempt to develop this sort of model in detail: at this stage, we mention it simply as a plausible possibility, and an indication that the available polarization observations, taken at face value, still do not present an insuperable objection to an interpretation of the FSC in terms of distributed sources rather than a single central source.

6.1.2 Morphology

If the FSC were due to scattering from a central source hidden by an obscuring torus, its intrinsic morphology would be essentially biconical. On the other hand, if it were due to star formation, we would expect it to show a distribution reflecting that of the molecular gas, which would not be likely to mimic a scattering geometry (unless, perhaps, the star formation were precipitated by phenomena associated

with the radio jet). At low resolutions, the appearance of the FSC *does* suggest a biconical morphology: this fact was largely responsible for the bipolar-nebula analogy put forward by Pierce & Stockton (1986); however, in our images (particularly our HRCam v' image), as well as in the best image of Vestergaard & Barthel (1993), the FSC has a spiral-like morphology, and it is thus less obviously consistent with a scattering model.

To what extent is this apparent morphology of the FSC determined by extinction? While we have emphasized the absence of significant local reddening over some regions of the FSC, we have also seen that low reddening may sometimes coexist with substantial extinction. Some parts of the FSC must certainly be obscured: the evidence for obscuration we see of the inner regions of the elliptical component virtually guarantees that any centrally concentrated part of the FSC will suffer substantial extinction. Furthermore, if we compare the positions of the peaks of the double structure of the FSC in our optical images with the structure in our nucleus-subtracted K' image (and assume that they refer to the same physical components), we find the latter to have a significantly smaller separation (1".5 vs 2".1). Unless there is a change in intrinsic color, this behavior implies that the inner regions of the FSC are obscured and have higher intrinsic surface brightness than the regions visible in the optical images. The crucial question is whether the "Z-shaped" morphology of the FSC [as seen in Fig. 4 of Vestergaard & Barthel (1993), and evident in both the upper-right inserts of Figs. 5(b), 5(c), and 5(d) and in Fig. 9(i)] is intrinsic or wholly the consequence of extinction. Certainly the shape seems to be due at least partly to two fingers of extinction coming in tangentially to the nucleus from the NE and SW, which are seen in the K' image [Fig. 5(e)] as well. But if these are responsible for the apparent spiral-like morphology (and it is not clear they are the whole story), they would also be responsible for the impression of a biconical structure at lower resolutions. Furthermore, in their symmetry around the nucleus, these dust lanes are themselves reminiscent of features seen in the inner regions of many spirals: see, e.g., the illustrations of the central part of M101 (Plate 31) and of SBb galaxies (Plates 45 and 46) in The Hubble Atlas of Galaxies (Sandage 1961). These suggest the presence of at least a spiral dust component and lend plausibility to one's naive impression that the FSC itself has a spiral-like morphology: one can fairly easily picture the dust lane just north of the center as being on the inner edge of the northwestern arm, which would be the more distant from us. This orientation would be consistent with the plane of the spiral structure being roughly perpendicular to the radio axis, since both the VLBI and large-scale jet structure indicate that the northwestern radio lobe is closer to us (Carilli *et al.* 1991).

6.1.3 The absence of broad lines

As discussed in Sec. *5.1*, no evidence for scattered broad Balmer lines has been detected either in the polarized component (Jackson & Tadhunter 1993) or in the total intensity spectrum (this work). If broad lines are indeed absent from the spectrum of the FSC, there would seem to be only three general categories of explanation: first, that Cyg A does not have a broad-line region; second, that Cyg A does have a broad-line region, but its light is not scattered into our line of sight; third, that light from the broad-line region is scattered, but the scattering process itself alters the spectrum so that the broad lines are undetectible.

It is difficult to imagine a formulation of strong unification of quasars and FR II radio galaxies (e.g., Barthel 1989) that could easily admit that Cyg A does not have a broad-line region. Cyg A is in some sense the classic example of the type of radio galaxy that, because of strong similarities in radio structure, should (under the unified hypothesis) contain a quasar (we discuss other evidence for a quasar nucleus in Cyg A in Sec. *6.3*); and, if quasars without broad-line regions exist at all, they are certainly extremely rare.[3] Even so-called "narrow-line quasars" have as much flux in their broad-line components as do normal quasars (Baldwin *et al.* 1988).

The possibility that the quasar continuum radiation is scattered, while light from the broad-line region is not, seems even more remote. Quasars essentially always show broad-line regions, and the broad-line equivalent widths show little dispersion from object to object (Yee 1980); these facts are inconsistent with any significant selective shadowing.

Any scattered broad lines could be washed out if the scattering were by hot electrons, as suggested by Fabian (1989) for the extended aligned components of high-redshift radio galaxies [although it is not clear that electron scattering is consistent with the polarization measurements of di Serego Aligieri *et al.* (1989) for 3C368 or Jannuzi & Elston (1991) for 3C265]. We estimate that with our present spectra, we probably would not be able to detect average quasar broad lines smeared by electrons hotter than $\sim 5\times10^6$ K. In Cyg A, unlike the high-redshift radio galaxies, the presumed scattering all occurs within a radius of $\sim$3 kpc, where the density of the hot gas should not be changing rapidly. Even if the density of the hot gas were as high as 1 cm^{-3} (if gas at 10^7 K were in pressure equilibrium with the emission-line clouds, densities of $\sim$0.3 cm^{-3} would be more reasonable), the optical depth for electron scattering out to this radius would be only about 5×10^{-3}, so essentially all of the radiation passes through. We then have a difficulty explaining why the observed FSC has such sharp edges and, in general, why we do not see scattered radiation at larger radii. Beyond the core, the density of the hot gas is expected to decline as r^{-1} (Fabian 1989), so the surface brightness of scattered radiation from a filled cone (or a conical shell formed from the differential volume of two cones with a common vertex) with its axis in the plane of the sky should be nearly constant. In short, the large scale height of the hot gas and the inefficiency of electron scattering mean that small, concentrated regions of scattering near the center are difficult to explain by this mechanism. Dust scattering does not have these problems; in fact, the correlation between the extent of the FSC and the region of strong extinction of the elliptical

[3]Blazars with weak or absent broad lines are irrelevant to this point: either, as commonly believed, they are to be subsumed into the unified scenario, in which case their beamed radiation is confined to a solid angle that makes a minor contribution to the scattered component and, in any case, cannot account for the apparent opening angle of the FSC in Cyg A; or their intrinsic radio properties isolate them from FR 2 radio galaxies and quasars.

component suggests that, if the FSC results from scattering, the scattering is almost certainly due to dust. Jackson & Tadhunter (1993) have arrived at the same conclusion on spectropolarimetric grounds.

The recent discovery of scattered broad Mg II λ2798 in Cyg A (Antonucci *et al.* 1994) looks convincing to us. If it is indeed correct, this detection resolves many of the questions discussed above. It shows that Cyg A does have a quasar nucleus and that the scattering is most likely due to dust or (less probably, in our opinion) cool electrons. Note, however, that [as Antonucci *et al.* (1994) emphasize] the confirmation that there is, after all, a component scattered from a quasar nucleus does not alter the fact that the bulk of the FSC radiation cannot be explained in this way.

6.1.4 Free–free emission

Antonucci *et al.* (1994) speculate that the FSC may be free–free emission, a possibility also mentioned by the anonymous referee. Figure 6 shows that free–free emission can have a spectral-energy distribution consistent with that observed for the FSC. We now consider this possibility in greater detail.

We note first that the fact that the FSC is resolved and extends over a few kpc differentiates this discussion from those of free–free emission in QSOs generally, where the emission is presumed to come from the accretion disk surrounding a supermassive nucleus (e.g., Barvainis 1993). In Cyg A, we assume that the plasma responsible for the free–free emission is at densities no higher than that required for pressure equilibrium with the $\sim 10^4$ K emission-line gas found in the same region as the FSC. From the average of the [S II] λλ6716,6731 ratios for the nuclear and NW emission-line clouds, we have found $N_e \approx 300$ cm^{-3}, so $P \approx 4\times10^{-10}$ dyn cm^{-2}. The plasma emitting the free–free emission cannot be cooler than $\sim 10^5$ K without a Balmer edge from free–bound transitions becoming noticeable, so we consider temperatures in the range 10^5–10^7 K. The free–free emissivity is given by

$$j_\nu = 5.4 \times 10^{-39} \frac{N_p N_e}{T^{1/2}} e^{-h\nu/kT} g_{ff} \text{ erg cm}^{-3}\text{ s}^{-1}\text{ Hz}^{-1}\text{ sr}^{-1}$$

(e.g., Osterbrock 1989), where we have assumed for simplicity a pure hydrogen composition, and $g_{ff} = g_{ff}(\nu, T)$ is the appropriate Gaunt factor. We have approximated g_{ff} by an analytic parametrization $g_{ff} \approx -1.1 \log(h\nu/kT) + 0.7$, which is an adequate fit to the curves given by Karzas & Latter (1961) over the temperature and frequency range we consider.

From the flux densities in a 5″ aperture given in Table 2, we estimate a flux density for the FSC at 5000 Å of 7.5×10^{-28} erg cm^{-2} s^{-1} Hz^{-1}, which gives a monochromatic luminosity $L_{5000} = 4.5\times10^{27}$ erg s^{-1} Hz^{-1}. For a plasma at 10^7 K, pressure equilibrium with the emission-line clouds implies a density of 0.3 cm^{-3}, and $j_\nu = 5.5\times10^{-43}$ erg cm^{-3} s^{-1} Hz^{-1} sr^{-1}. Comparing this volume emissivity with the luminosity given above gives a characteristic volume of 6.5×10^{68} cm^3, equivalent to a sphere with a radius of 17 kpc. Since the observations refer to a region <3 kpc in radius, the surface brightness of the FSC is a factor of ~30 too high to be consistent with free–free emission at this temperature and density.

At lower temperatures, this discrepancy disappears: e.g., a 10^6 K plasma in pressure equilibrium with the emission-line gas ($n_e = 3$ cm^{-3}) can be just consistent with the observed surface brightness. However, the total mass of the plasma would be $8\times10^9 M_\odot$, and the cooling time for solar abundance material would be only a few 10^4 yr, giving mass flow rates $>10^5 M_\odot$ yr^{-1}. Furthermore, this large mass flow rate implies that at any given time there will exist a pool of plasma with $T \sim 10^6$ K, resulting in the emission of $\gtrsim 3\times10^{42}$ erg s^{-1} in the [Fe X] λ6374 line (Voit *et al.* 1994). If we take our highest upper limit for [Fe X]/Hβ multiplied by the total Hβ luminosity over our centered 5″ aperture (which effectively gives a conservative upper limit to the [Fe X] emission), we obtain a value nearly 1000 times lower. The fact that the gas in this temperature range may be cooling isochorically and would not then be in pressure equilibrium cannot help much: one can increase the cooling time—and therefore decrease both the mass-flow rate and the [Fe X] emission—at lower densities, but then the surface brightness of the free–free emission is again too low. Even at 10^5 K, at the lowest density consistent with the observed surface brightness, we estimate mass-flow rates $>10^4 M_\odot$ yr^{-1} and predict [Fe X] λ6374 intensities nearly 100 times our upper limit.

In summary, any attempt to explain the FSC as being largely free–free emission from a diffuse component appears to fail from a combination of (1) the absence of a Balmer edge, (2) surface brightness constraints, and (3) the weakness of [Fe X] λ6375.

6.1.5 Evidence for star formation in a central disk

The attractive elegance and general success of a scenario that consolidates quasars and FR II radio galaxies into a single population [Barthel (1989); see also Antonucci (1993) for a recent review of unified models in general] has ensured a warm welcome for the suggestion by Pierce & Stockton (1986) that the inner double structure in Cyg A is scattered radiation from a hidden central source. We now believe this interpretation to be wrong, in spite of other evidence that favors the presence of a hidden quasar nucleus in Cyg A. To summarize our main points:

First, the prediction of Pierce & Stockton (1986) that the FSC would show high polarization has not been confirmed. While the proper interpretation of the small polarization that is present certainly has not been nailed down securely, we believe that our evidence that a large portion of the radiation from the late-type stellar component in the central region is *locally* scattered suggests that polarization in the FSC and emission lines may also be due to such local scattering.

Second, the picture put forward by Pierce & Stockton (1986) was strongly motivated by morphology: not only was the FSC extended, but its shape could plausibly be interpreted as essentially biconical. Our higher-resolution observations show a mini-spiral morphology and dust lanes tangential to the nucleus instead; these are much more likely to

arise from star formation than from scattering of a central source.

Finally, the only reasonable candidate for the presumed central source is a quasar nucleus. Our spectroscopy and that of Jackson & Tadhunter (1993) put stringent limits on the presence of scattered broad lines in the optical total intensity and polarized components of the FSC, respectively. We argue that attributing the lack of visible broad lines to scattering by hot electrons leads to an inconsistency with the observed morphology. The detection of broad Mg II by Antonucci *et al.* (1994), while demonstrating that a quasar nucleus and scattered radiation from it are both present, also reinforces the argument that the FSC seen in the optical cannot be primarily due to such radiation.

One observation that might be considered consistent with the central scattering hypothesis is the close agreement between the morphology of the brightest region of the ionized gas distribution and the NW component of the FSC, which clearly invites interpretation as a cloud of dust and gas lying within the cone of direct illumination by the central source. The emission-line counterpart of the brighter SE FSC component is weaker and less well defined, but still shows reasonable correspondence. However, this agreement between the FSC and ionized gas distributions can also be consistent with the distribution of young stars following the density distribution of the gas, even if (as we have argued in Sec. 5.3) the gas is photoionized mostly by the central source rather than by the stars; in this case, the observed distribution of the ionized gas is controlled both by whether the gas has a direct view of the UV continuum source and by the density distribution of the gas itself.

We have concentrated on reasons for doubting that the FSC arises from scattering from an obscured central source, but we believe that the morphological evidence points to a clear alternative. The large quantities of dust in the central regions, the symmetric pattern of obscuration near the nucleus, and the mini-spiral morphology of the FSC all support the conclusion that the FSC is the result of a starburst in a disk of gas in the center of Cyg A.

6.2 A Recent Merger?

The idea that much of the activity we see in Cyg A is due to a collision or merger of galaxies goes all the way back to Baade & Minkowski (1954), although their specific model is no longer tenable. More recent suggestions along this line have been made by Thompson (1984), Pierce & Stockton (1986), and Baum *et al.* (1992). New impetus to the idea that mergers, starbursts, and nuclear activity may, under certain circumstances, all be connected is provided by observational work on luminous IR galaxies (Sanders *et al.* 1988) and recent modeling of mergers that shows that the gas quickly looses angular momentum and settles towards the center (Barnes & Hernquist 1991; Hernquist & Barnes 1991). A starburst in the center of Cyg A is consistent with a merger, but can hardly be considered unambiguous evidence for one. The velocity field we observe for the gas, however, seems to us to be more compelling.

Aside from the weak, high-velocity components apparently associated with the radio jets, the kinematics of the ionized gas, as described in Sec. *5.2* and shown in Figs. 13 and 14, give every indication of being gravitationally dominated. Nevertheless, the global velocity field certainly does not reflect a stable equilibrium situation. The coexistence of ordered, coherent velocity structure in individual components with a general lack of order globally (i.e., velocity reversals, discontinuities, double components, etc.) is reminiscent of the kinematics of the gas in ongoing mergers like NGC 7252 (Schweizer 1982; Wang *et al.* 1992). In particular, the apparent counter-rotation of the gas superposed on the nucleus relative to the general trend of the gas elsewhere is strong circumstantial evidence for a recent merger.

At least at first sight, there is no obvious evidence for corroborating tidal tails or shells; even if they were present, typical shells like those seen around some nearby ellipticals are so narrow and of such low contrast that they would be very difficult to detect at the distance of Cyg A. However, there have been suspicions that something strange has taken place in the NW quadrant of the inner region in Cyg A (see, e.g., Thompson 1984). The arc of emission-line gas extending to the SW from the bright emission peak NW of the nucleus has a somewhat tail-like appearance, but our deconvolved [O III] image [Fig. 9(b)] could equally be taken to support a filament extending to the SW, then back to the NE to connect to the nuclear emission region: i.e., a curved bridge- or arm-like structure, viewed close to its own plane. However, this sort of scenario would seem to be difficult to reconcile with the gas velocities. Regardless of the final outcome of such morphological supporting evidence, we are intrigued about the nature of the secondary K' peak, located $\sim 1\farcs3$ N of the nucleus, on the NE edge of the bright emission-line peak. Could it be a relic nucleus of a companion that has not yet fully merged with the main body of Cyg A? If so, the spiral pattern seen in the FSC may have been induced by its passage. However, it is difficult to see how such a scenario can simultaneously make sense of both the morphology and the velocity field of the gaseous component, where we see a spiral-like structure but discontinuous and contradictory velocity trends. Fairly sophisticated modeling will be required to determine whether a consistent picture incorporating all of these elements is possible.

On a somewhat larger scale, the faint, ragged low-ionization gaseous structure crossing Cyg A from S to NE could be the stripped remains of a disk that has not yet fallen in. An alternative possibility is that it is material deposited from the inferred cooling flow around Cyg A (Arnaud *et al.* 1984). However, the association of considerable dust with this gas would seem to make such an origin unlikely, since the dust could not be expected to survive a long period in the hot phase. While there seems to be dust in line-emitting filaments associated with cooling flows, Donahue & Voit (1993) cite its presence as evidence that the gas in these filaments was never at high temperatures, rather than as evidence that the dust can somehow survive in such environments. We suspect that in the present case the material is tidal debris, but that the pressure of the x-ray-emitting gas may have helped confine and preserve the 10^4 K gas clouds against self destruction by free expansion.

6.3 Is There a Hidden Quasar in Cygnus A?

In suggesting that the FSC is not scattered quasar radiation, we are not denying the presence of a quasar nucleus in Cyg A; we are only arguing that the question has to be decided on other evidence. In our view, the evidence in favor is now quite compelling:

(1) As we have discussed in Sec. *5.3*, the relative emission line strengths and wide range of ionization present in Cyg A place it clearly in the power-law photoionized region of line-ratio diagnostic diagrams. Even the low-ionization gas to the S and NE is plausibly explained in terms of x-ray photoionization with a low ionization parameter.

(2) Arnaud *et al.* (1987) and Koyama (1992) have directly detected an unresolved hard x-ray nucleus, which provides direct evidence for an active nucleus.

(3) Even though we believe that we barely resolve the K' nucleus, and therefore that it cannot be the quasar nucleus itself, it is not at all implausible that it is due to hot dust in the immediate vicinity of a quasar nucleus.

(4) Finally, the recent detection of broad Mg II λ2798 by Antonucci *et al.* (1994) leaves little doubt that a quasar nucleus is present.

Assuming that the quasar is responsible for photoionizing the observed extended emission, how luminous does it have to be? Taking the Balmer line fluxes for a 5″ diameter aperture centered on the nucleus, as given in Table 2, and correcting them for standard extinction in the amount needed to restore a Case B ratio, we obtain an Hβ flux of 9×10^{-14} erg cm^{-2} s^{-1}, which corresponds to an Hβ luminosity of 6×10^{41} erg s^{-1} (H_0=75 km s^{-1} Mpc^{-1}). Using the relation between the Hβ luminosity and the Lyman continuum luminosity density given by Fosbury *et al.* (1982), assuming that the spectral index α near the Lyman limit is ~-1, and assuming for the moment that the ionized gas is radiation bounded and completely covers the source, we find L(912 Å)$=2.3\times10^{28}$ erg cm^{-2} s^{-1} Hz^{-1}. Again assuming $\alpha\sim-1$ between 4000 Å and the Lyman limit, we obtain $L(B)\sim10^{29}$ erg s^{-1} Hz^{-1}, which, for a typical quasar SED (Sanders *et al.* 1990), corresponds to $L_{\rm bol}\sim1.3\times10^{45}$ erg s^{-1}. If our line of sight were within one of the unobscured cones, we would then expect to see a quasar nucleus with $B\sim16$.

Remember, however, that we have assumed that the extended gas has a covering factor of unity, which is almost certainly not the case. For a sample of ten low-redshift quasars showing extended emission, estimated covering factors *of the extended gas only* ranged from 0.1% to 4%, with a median of 0.7% (Stockton & MacKenty 1987). For Cyg A, our line fluxes no doubt include more of the inner gas than do the quasar measurements; but the important point is that our estimates of the quasar luminosity are almost certainly lower limits and could easily be underestimates by a factor of ~10 or more.

6.4 Alignment of Optical and Radio Structure

The most intriguing of the ways in which powerful radio galaxies at high redshift differ from most radio galaxies at low redshifts is in the alignment between the optical and radio structure (Chambers *et al.* 1987; McCarthy *et al.* 1987; Rigler *et al.* 1992). Whatever the physical mechanism behind this effect, it has generally been assumed that its main dependence is on cosmic epoch and that the lack of such alignment in radio galaxies at low redshifts is somehow due to evolution of the environments in which radio galaxies are found. However, this "alignment effect" was discovered and substantiated almost entirely by comparing powerful radio galaxies at high redshifts with much less powerful radio galaxies at low redshifts: it therefore has always been possible that the principal correlation is with radio power rather than with epoch. The question will be settled finally by observations of complete samples of less powerful radio galaxies at high redshift, but already there is at least one substantial claim that the dominant dependence is indeed on radio power (Dunlop & Peacock 1993). Cygnus A, as a single object, may not add much weight to the argument, but it is the only low-redshift radio galaxy with a radio power comparable to the high-redshift radio galaxies for which the alignment effect is well established.

First, one has to sort out exactly what is meant by "the alignment effect." The term has been used to describe a range of optical morphologies, from a rather smooth, continuous elongated distribution (e.g., 3C352), through various degrees of aligned lumpy structure (3C368, 3C324, 3C265), to cases where a single discrete object lies roughly along the radio axis (e.g., 3C356). It is not clear that the same physical mechanism is operative in all of these cases. Some powerful radio galaxies at $z\sim1$ do not show an appreciable alignment effect at all (e.g., Rigler *et al.* 1992). There is also some confusion in the literature regarding the alignment at different wavelengths. In spite of suggestions that only the ionized gas is aligned (Meisenheimer & Hippelein 1992; Hippelein & Meisenheimer 1992), deep imaging through line-free filters leaves no doubt that the continuum radiation is also aligned, and that the aligned component becomes more dominant at shorter wavelengths [Rigler *et al.* (1992); see also the recent review by McCarthy (1993)]. However, Dunlop & Peacock (1993) find that the degree of alignment between the IR and radio axes is significantly more precise than that between the optical and radio axes, and they suggest that different mechanisms may be operative in the two wavelength regimes. Briefly, they discount suggestions that the continuum comes from jet-induced star formation (Rees 1989; Chambers & McCarthy 1990) because of difficulties in reconciling the observed SED with a stellar population young enough to be consistent with the inferred age of the radio source [but see Hammer *et al.* (1993) for another view]. Interpretations based on either Compton scattering of microwave background photons or local heating of the gas by low-energy relativistic electrons (Daly 1992) can explain the majority of cases where the optical and radio extensions are not perfectly aligned only if one invokes a spectrally aged electron distribution present where the optical emission is seen—presumably from a previous or precessing radio jet. Models based on scattering of radiation from a hidden central source are supported by high polarizations found in several objects (di Serego Aligieri *et al.* 1989; Jannuzi & Elston 1991; Tadhunter *et al.* 1992). The degree of misalignment between the optical and radio axes and the tendency of the

aligned continuum component to show a better correlation with the extended ionized gas than with the radio structure are consistent with this model, because the relative numbers of quasars and radio galaxies observed suggest an opening angle for direct viewing of the quasar of around 70° to 90°, for strong unification of the two classes. This means that, within this cone, the detailed alignment of both the scattered quasar radiation and the gas ionized by the UV continuum will be controlled by the distribution of matter, while a gross tendency to be aligned with the radio axis is maintained by the coincidence of the axis of the cone and the radio axis. In the context of the unified scenario, the better alignment of the IR structure could be the result of the narrower cone in which the (redder) blazar continuum is beamed (Dunlop & Peacock 1993).

How does Cyg A fit into this picture? We have noted some alignments between optical components and the radio structure: the brightest emission line cloud lies roughly in the direction of the radio jet, and the relative distributions of the high-ionization gas and the lower ionization gas show the former to be aligned along the radio axis. It is entirely possible, and even likely, that this alignment of the ionized gas in Cyg A is a miniature version of what is happening in the powerful radio galaxies at high redshifts. In both cases, the radiation from the central UV continuum source likely escapes more freely along cones aligned with the radio structure.

It has also long been noted that a line connecting the double structure of the FSC lies close to the radio axis. A comparison of this structure with aligned continuum components at high redshift is complicated by our generally viewing high-redshift radio galaxies in the rest-frame UV, where we currently have only sketchy observations of Cyg A. We suspect that what we see in Cyg A in the optical may have a different physical origin from that of aligned structure in high-redshift radio galaxies. Certainly, if we are correct in attributing polarization in Cyg A to scattering of distributed sources, it is quite likely that both the polarization mechanism and the nature of the flat-spectrum components are different in the two cases. The situation may be quite different in the UV. There is tentative evidence that the polarization is higher in the UV than in the optical (Antonucci *et al.* 1994), and it will be of interest to see how the inner morphology of Cyg A appears at ~2500 Å, i.e., roughly the spectral region sampled by the B filter in $z\sim1$ radio galaxies.

Even so, it is already clear from our u filter observations, which correspond to an observed wavelength of ~6400 Å at $z\sim1$, that the amplitude of the continuum alignment in Cyg A is not nearly as pronounced as that of the more extreme high-redshift galaxies. The same applies to the emission-line alignment; in fact, it is doubtful that either alignment would be detectible in ground-based observations if Cyg A were removed to $z\sim1$.

7. SUMMARY

7.1 A Toy Model of Cygnus A

The central region of Cyg A is a complex mixture of ionized gas, featureless continuum component, and dust. Reflecting this complexity, much of our discussion has had to be hedged with qualifications and caveats. Here we propose to ignore such uncertainties and simply outline a model, schematic and certainly incomplete, but one which is consistent with the preponderance of the evidence we have presented and with our current understanding of Cyg A from other work. While we would like to hope that the main outlines of this picture will survive future investigations unscathed, the history of previous interpretations of Cyg A is not terribly encouraging. A more modest hope is that by presenting a definite model, we will more clearly highlight areas in which the picture is uncertain or incomplete, and therefore help to focus future work.

We begin with the nucleus. From the evidence for broad Mg II, a hard unresolved x-ray source, and a flat photoionizing continuum, and assuming that the extended ionized gas intercepts ~10% of the Lyman continuum radiation, we place a quasar with $L_{\rm bol}\sim10^{46}$ erg s^{-1} at the center of our model. We assume that the K' nucleus is coincident with this quasar (and with the compact radio source) because it must suffer less extinction than the central components seen in the optical continuum and emission lines, and because it is only barely resolved. However, we are not seeing the quasar directly, even at K', but rather dust at radii of 100–200 pc from the center.

The central peaks seen in our optical continuum and emission-line images are coincident with each other, within the errors, but are centered about 0.2″ W of the the IR peak and are clearly elongated NE–SW. Both the centering and the elongation may be partly due to obscuration, although it is significant that the velocity gradient of the nuclear ionized gas is roughly in the direction of elongation. We do believe that these peaks are from stars and gas actually near the nucleus and not simply superposed on it, and the counter-rotation of this gas relative to the general trend in the rest of Cyg A is one of our primary arguments for a recent merger in Cyg A.

We identify the secondary K' peak, at a projected distance of 1.″3 (=1.3 kpc) N of the nucleus, as the compact nucleus of a merging companion: some of the gas has already settled to the center, forming the counter-rotating disk, but the nucleus still has not fully merged. The extensions of low-ionization gas to the S and NE are part of an irregular disk or loop seen close to edge on. We see dust associated with at least the projection to the S, and we interpret the whole structure as being a portion of the disk of the merging gas-rich companion.

The flat-spectrum component, comprising the optical continuum peaks SE and NW of the nucleus, results from a population of young stars comprising the mini-spiral morphology seen in our optical continuum images. The spiral effect is enhanced by prominent dust lanes approaching the nucleus tangentially from the NE and SW along the inner edge of the spiral "arms."

Differences in ionization can be understood qualitatively in terms of anisotropic emission of the UV continuum. In the biconical region roughly centered on the radio axis, in which the quasar continuum source can be viewed directly, we see strong [O III] emission. Elsewhere, the ionization parameter

is low because only x-rays with energies $\gtrsim 3$ kev get through, and a LINER-like spectrum results.

While most of the kinematics of the ionized gas seem dominated by gravitation, the high-velocity components on the E and especially the W side of the nucleus are almost certainly connected with the radio jets, which also have affected the morphology of the main distribution of low-velocity [O III]-emitting gas.

7.2 Unresolved Issues and Future Work

As is often the case with an investigation into a complex phenomenon, this study has probably raised more questions than it has answered. We mention here only a few of these that we feel are ripe for further work:

It would be helpful to have a reasonably precise separation of the FSC and the elliptical component for at least one wavelength. Probably the best hope would be to take narrow band, emission-line-free images on both sides of the 4000 Å break. A properly scaled difference between these should give an accurate morphology of the FSC alone, allowing the determination of an similarly accurate map of the extinction of the elliptical component in the inner few arcsec.

Our marginal resolution of the IR nucleus needs confirmation, and further investigation of the secondary IR peak is needed. Both of these goals could best be accomplished by deep, high-resolution imaging in the *L* band.

Our suggestion that the observed amplitudes and position angles of polarization in Cyg A could be produced by scattering of distributed sources embedded in dust needs to be confirmed by constructing a plausible scattering model. Similarly, while we believe that the velocity field of the gas is strong evidence for a merger, a specific model of the interaction is needed to test whether the secondary IR nucleus, the counter-rotating nuclear gas, and the outer belt of low-ionization gas can be incorporated into a self-consistent picture.

Our views on Cygnus A have been influenced by discussions over the years with many people; we are grateful to them all for their time and interest. Special thanks go to Joss Bland-Hawthorn, who, after a discussion, took the time to write up his detailed reflections and send them to us; and also to Esther Hu for discussions and written comments on a portion of the paper. Peter Barthel, and Clive Tadhunter sent us preprints of their own recent work on Cygnus A, as did Ski Antonucci, who also kindly read and commented on an early draft. We appreciate conversations with Leon Lucy and Richard Hook on deconvolution; the latter also supplied us with his latest versions of IRAF implementations of deconvolution software. Francesco Valdes straightened out some problems we were having with spectral reductions. A.S. thanks Professor Richard Ellis for arranging an extended visit to the Physics Department at the University of Durham during the period when most of the data reduction and writing were done; he is also grateful for continued support by the NSF for this work under Grants Nos. AST8715330 and AST9221909.

REFERENCES

Antonucci, R. 1993, ARA&A, 31, 473
Antonucci, R., Hurt, T., & Kinney, A. 1994, preprint
Antonucci, R., & Barvainis, R. 1990, ApJ, 363, L17
Arnaud, K. A., Fabian, A. C., Eales, S. A., Jones, C., & Forman, W. 1984, MNRAS, 211, 981
Arnaud, K. A., Johnstone, R. M., Fabian, A. C., Crawford, C. S., Nulsen, P. E. J., Shafer, R. A., & Mushotzky, R. F. 1987, MNRAS, 227, 241
Baade, W., & Minkowski, R. 1954, ApJ, 119, 206
Baldwin, J. A. 1975, ApJ, 201, 26
Baldwin, J. A., Phillips, M. M., & Terlevich, R. J. 1981, PASP, 93, 5
Baldwin, J. A., McMahon, R., Hazard, C., & Williams, R. E. 1988, ApJ, 327, 103
Barnes, J. E., & Hernquist, L. E. 1991, ApJ, 370, L65
Barthel, P. D. 1989, ApJ, 336, 606
Barvainis, R. 1993, ApJ, 412, 513
Baum, S. A., Heckman, T. M., & van Breugel, W. 1992, ApJ, 389, 208
Carilli, C. L., Bartel, N., & Linfield, R. P. 1991, AJ, 102, 1691
Carilli, C. L., Dreher, J. W., Conner, S., & Perley, R. A. 1989, AJ, 98, 513
Chambers, K. C., & McCarthy, P. J. 1990, ApJ, 354, L9
Chambers, K. C., Miley, G., & van Breugel, W. 1987, Nature, 329, 609
Coleman, G. D., Wu, C.-C., & Weedman, D. W. 1980, ApJS, 43, 393
Daly, R. A. 1992, ApJ, 399, 426
di Serego Aligieri, S., Fosbury, R. A. E., Quinn, P. J., & Tadhunter, C. N. 1989, Nature, 341, 307
Djorgovski, S., Weir, N., Matthews, K., & Graham, J. R. 1991, ApJ, 372, L67
Donahue, M., & Voit, G. M. 1993, ApJ, 414, L17
Dunlop, J. S., & Peacock, J. A. 1993, MNRAS (in press)
Fabian, A. C. 1989, MNRAS, 238, 41p
Ferland, G. J., & Netzer, H. 1983, ApJ, 264, 105
Ferland, G. J., & Osterbrock, D. E. 1985, ApJ, 289, 105
Fosbury, R. A. E., *et al.* 1982, MNRAS, 201, 991
Gaskell, C. M., & Ferland, G. J. 1984, PASP, 96, 393
Goodrich, R. W., & Miller, J. S. 1989, ApJ, 346, L21
Griffin, R. F. 1963, AJ, 68, 421
Gunn, J. E., & Stryker, L. L. 1983, ApJS, 52, 121
Hammer, F., Le Fèvre, O., & Angonin, M. C. 1993, Nature, 362, 324
Hernquist, L. E., & Barnes, J. E. 1991, Nature, 354, 210
Hippelein, H., & Meisenheimer, K. 1992, A&A, 264, 472
Hook, R., & Lucy, L. 1992, ST–ECF Newletter, 17, 10
Jackson, N., & Tadhunter, C. N. 1993, A&A (in press)
Jannuzi, B. T., & Elston, R. 1991, ApJ, 366, L69
Karzas, W., & Latter, R. 1961, ApJS, 6, 167
Koyama, K. 1992, in X-Ray Emission from Active Galactic Nuclei and the Cosmic X-Ray Background, MPE Report 235, edited by W. Brinkmann and J. Trümpler (MPE, Garching), p. 74
Kronberg, P., van den Bergh, S., & Button, S. 1977, AJ, 82, 315
Lilly, S. J., & Hill, G. J. 1987, ApJ, 315, L103
McCarthy, P. J., van Breugel, W., Spinrad, H., & Djorgovski, S. 1987, ApJ, 321, L29
McCarthy, P. J. 1993, ARA&A, 31, 639
Massey, P., Strobel, K., Barnes, J. V., & Anderson, E. 1988, ApJ, 328, 315
Meisenheimer, K., & Hippelein, H. 1992, A&A, 264, 455
Oke, J. B., & Gunn, J. E. 1983, ApJ, 266, 713
Osterbrock, D. E. 1983, PASP, 95, 12
Osterbrock, D. E. 1989, Astrophysics of Gaseous Nebulae and Active Galactic Nuclei (University Science Books, Mill Valley)
Osterbrock, D. E., & Miller, J. S. 1975, ApJ, 197, 535
Pierce, M. J., & Stockton, A. 1986, ApJ, 305, 204
Rees, M. J. 1989, MNRAS, 239, 1P
Rigler, M. A., Lilly, S. J., Stockton, A., Hammer, F., & Le Fèvre, O. 1992, ApJ, 385, 61

Sandage, A. 1961, The Hubble Atlas of Galaxies (Carnegie Institution of Washington, Washington)
Sanders, D. B., Phinney, E. S., Neugebauer, G., Soifer, B. T., & Matthews, K. 1990, ApJ, 347, 29
Sanders, D. B., Soifer, B. T., Elias, J. H., Madore, B. F., Matthews, K., Neugebauer, G., & Scoville, N. Z. 1988, ApJ, 325, 74
Schweizer, F. 1982, ApJ, 252, 455
Shaw, M., & Tadhunter, C. 1994, MNRAS (in press)
Shull, J. M., & McKee, C. J. 1979, ApJ, 227, 131
Spinrad, H., & Stauffer, J. R. 1982, MNRAS, 200, 153
Stockton, A., & MacKenty, J. W. 1987, ApJ, 316, 584
Tadhunter, C. N. 1991, MNRAS, 251, 46P
Tadhunter, C. N., Metz, S., & Robinson, A. 1994, MNRAS (in press)
Tadhunter, C. N., Scarrott, S. M., & Rolph, C. D. 1990, MNRAS, 246, 163
Tadhunter, C. N., Scarrott, S. M., Draper, P., & Rolph, C. 1992, MNRAS, 256, 53P
Thompson, L. A. 1984, ApJ, 279, L47
van den Bergh, S. 1976, ApJ, 210, L63
Veilleux, S., & Osterbrock, D. E. 1987, ApJS, 63, 295
Vestergaard, M., & Barthel, P. D. 1993, AJ, 105, 456
Voit, G. M., Donahue, M., & Slavin, J. D. 1994, ApJS (in press)
Wainscoat, R., & Cowie, L. L. 1992, AJ, 103, 332
Wang, Z., Schweizer, F., & Scoville, N. Z. 1992, ApJ, 396, 510
Ward, M. J., Blanco, P. R., Wilson, A. S., & Nishida, M. 1991, ApJ, 382, 115
Witt, A. N., Thronson, H. A., & Capuano, J. M. 1992, ApJ, 393, 611
Yee, H. K. C. 1980, ApJ, 241, 894
Yee, H. K. C., & Oke, J. B. 1978, ApJ, 226, 753

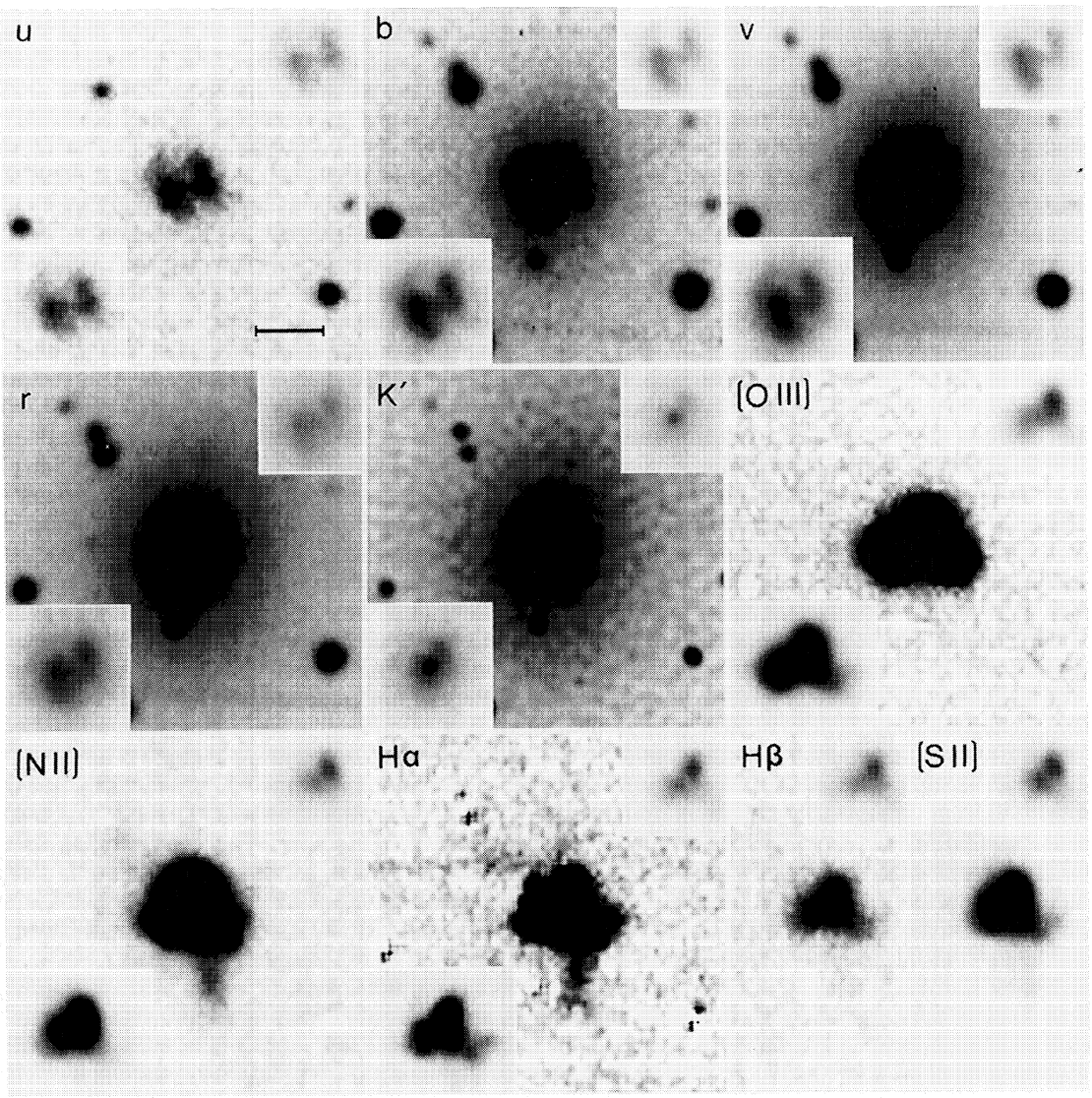

FIG. 2. Images of the inner regions of Cyg A. The first five panels show continuum images; filter designations are given in the upper-left corner, and the corresponding central wavelengths and FWHM are given in Table 1. The remaining panels are continuum-subtracted emission-line images. The scale bar is 4″ long. Insets show the central region at different contrasts and are centered on the IR nucleus, except for the lower-left inserts for the emission-line images, which have been extended to the west to show all of the bright emission. The streaks at the bottom of the *b*, *v*, and *r* images and at the left center of the Hα image are due to CCD column charge bleeding from nearby saturated stars.

Stockton *et al.* (see page 417)

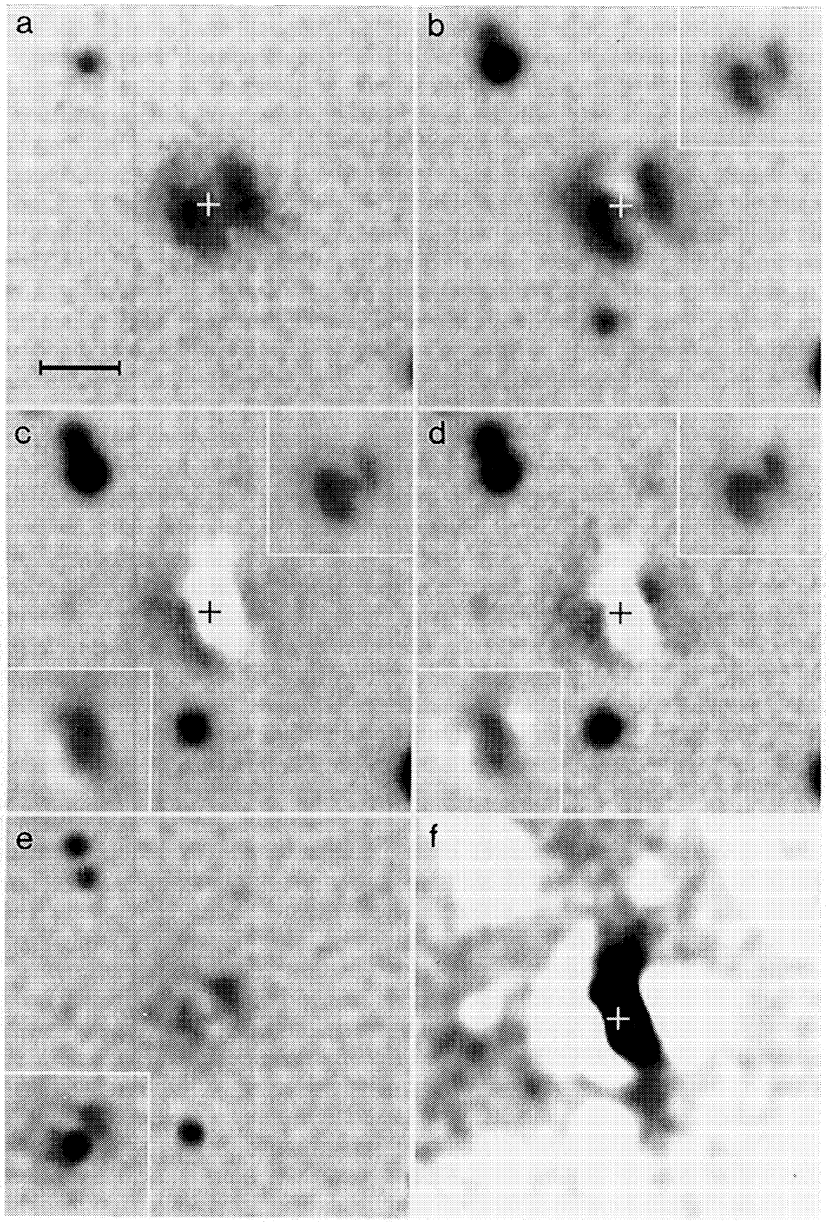

FIG. 5. Residual continuum images after subtracting K' elliptical model. Panels (a)–(e) show, respectively, the u, b, v, r, and K' images. Lower-left insets for v and r images have the gray scale inverted to show structure in the negative regions; that for K' image is a version of the model-subtracted image with the nucleus included. Upper-right insets show the original images after subtracting elliptically symmetric b, v, and r models. (f) High-contrast positive version of the sum of the v and r images, after smoothing with a Gaussian with σ=0.″3; note the extension of the dust to the S. Crosses indicate the position of the IR nucleus, which is also at the center of each inset. The scale bar is 4″ long.

Stockton *et al.* (see page 419)

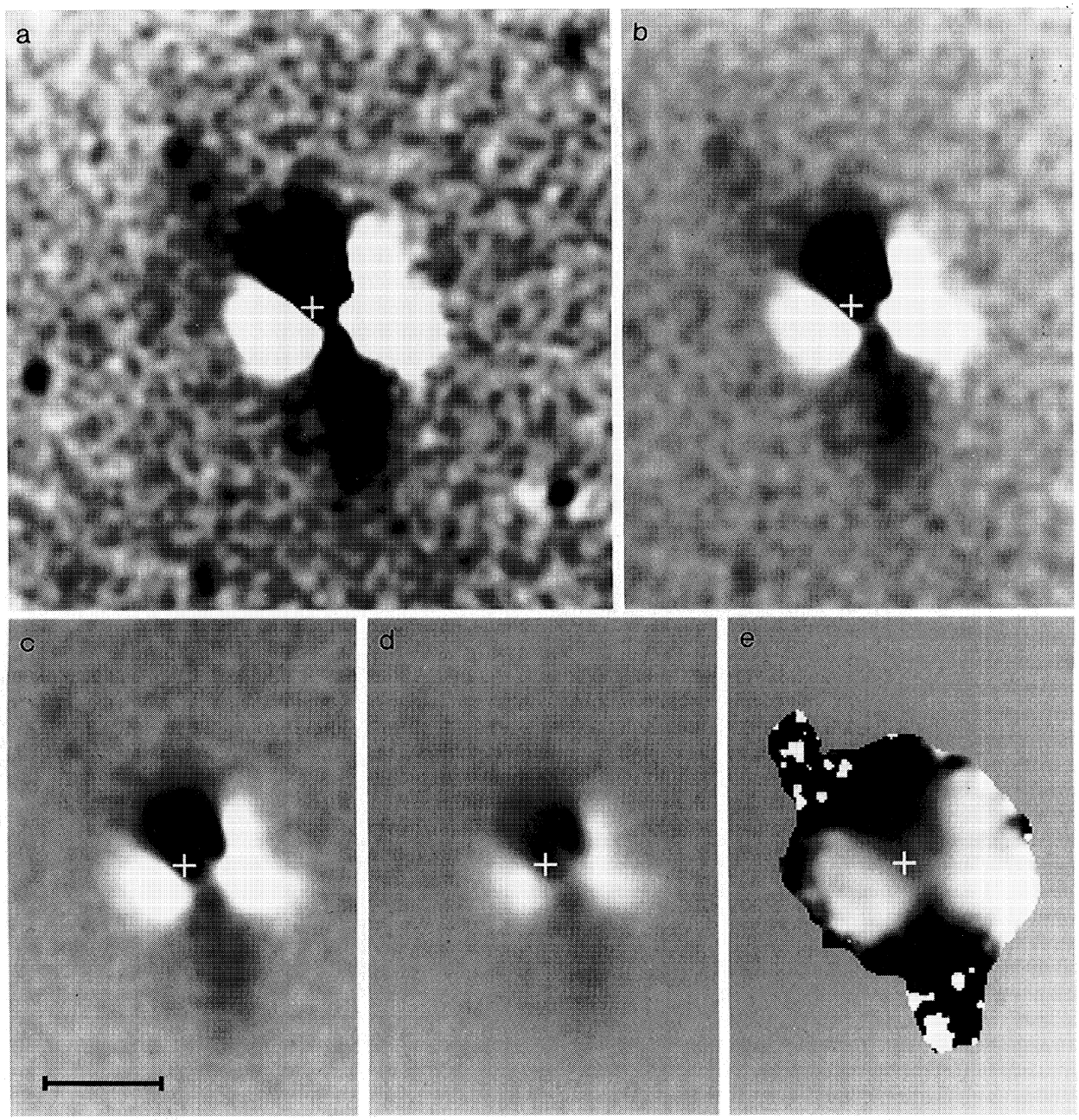

FIG. 8. (a) Differential brightness distributions for [O III] and [N II]. This image is the result of scaling the [N II] image to the [O III] image and subtracting. Regions strong in [N II] are darker on this plot; those strong in [O III] are lighter. (b),(c),(d) Lower-contrast versions of (a). (e) Ratio of [O III] image to [N II] image, after median filtering each with a 0.″9×0.″9 kernal. Again, strong [N II] regions are dark, strong [O III] regions, light; regions with little [N II] flux have been masked. In each case, the cross indicates the position of the IR nucleus, and the scale bar is 4″ long.

Stockton *et al.* (see page 422)

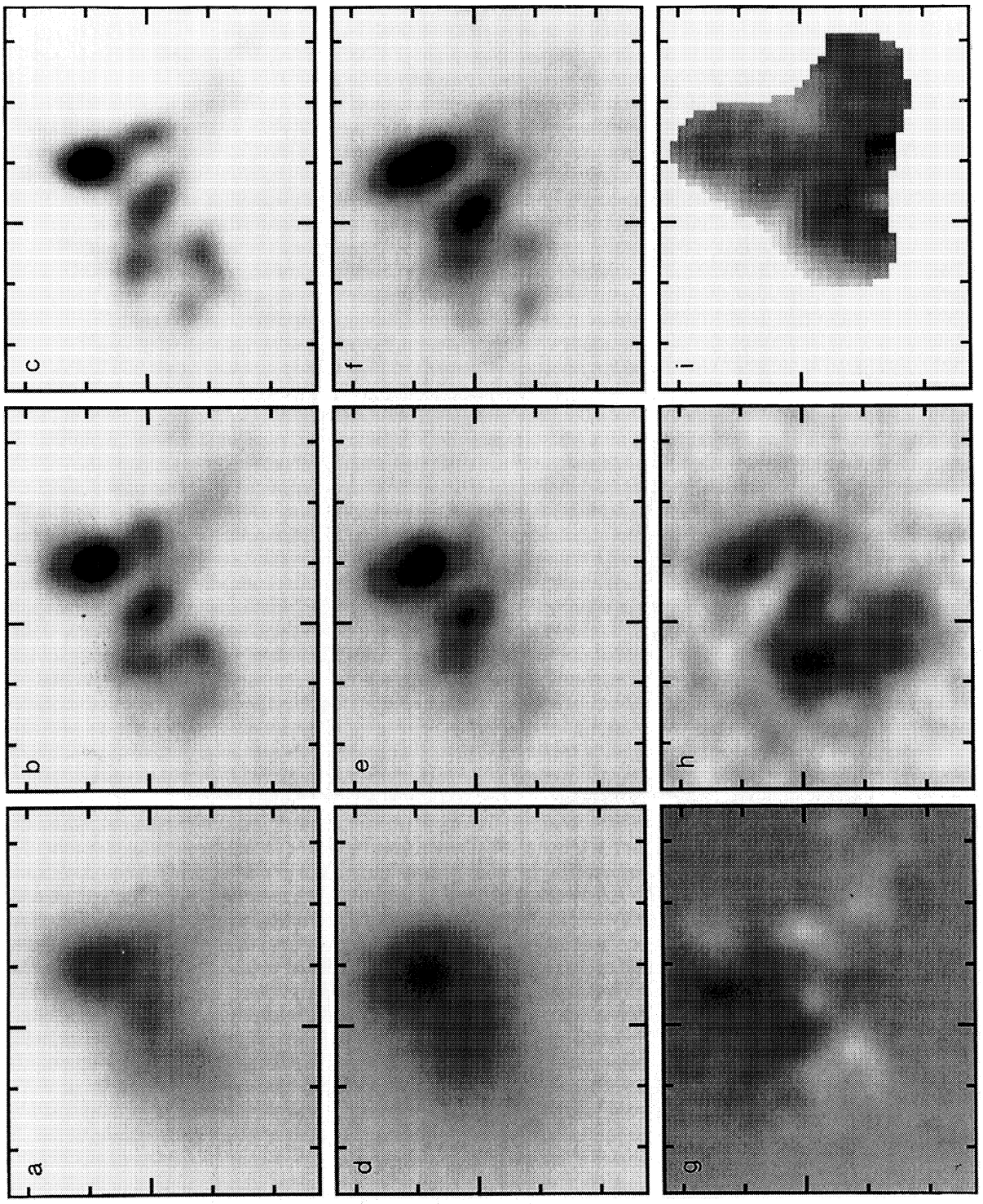

FIG. 9. High-resolution imaging of the central region of Cygnus A in [O III], [N II], and v' continuum. (a) Original HRCam [O III] image, FWHM 0".69; (b) HRCam [O III] image restored to a FWHM of 0".30; (c) deconvolution of our "standard" [O III] image (original FWHM 1".06) to a FWHM of 0".35. (d)–(f) Similar sequence for [N II]. (g) difference of [N II] image (e) and [O III] image (b). (h) HRCam v' line-free continuum image, FWHM 0".55. (i) Ratio of Hα to Hβ: darker regions indicate more reddening. Tickmarks are at 1" intervals, and the position of the IR nucleus is indicated by the longer marks.
Stockton *et al.* (see page 422)

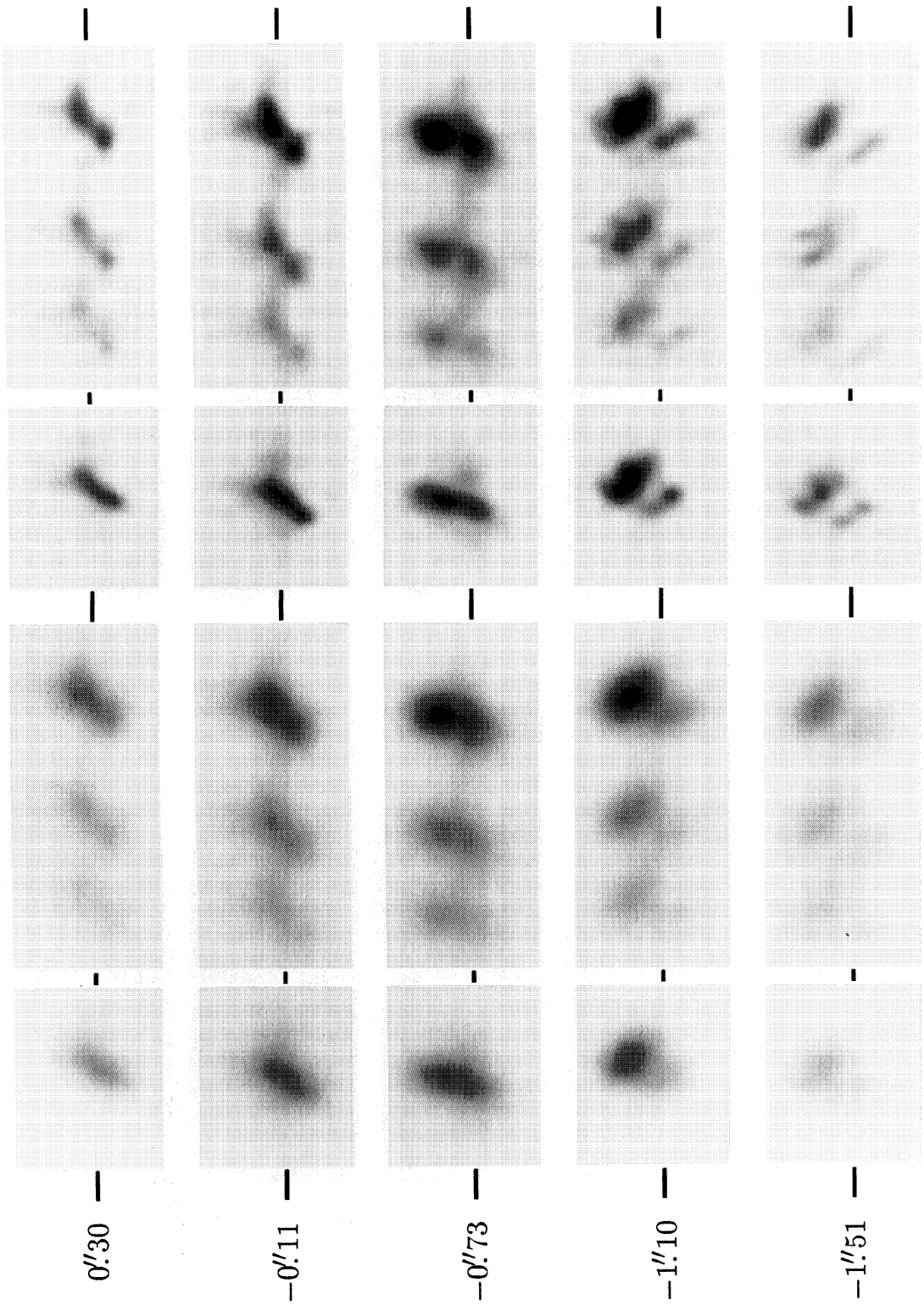

FIG. 14. Images of [O III] λ5007 and the Hα–[N II] lines in spectra covering the bright emission regions. All spectra were obtained with 0.″7 slits at PA 0°, and the region shown corresponds to a slit length of 5.″7. Slit offsets from the K' nucleus are given to the left of each set, and the horizontal lines indicate the nuclear position along the slit. The original spectra (rebinned to a finer grid) are shown on the left, and deconvolved spectra are shown on the right. The PSF for the Richardson–Lucy deconvolutions was derived from the profile of a star on the slit for the spatial coordinate and the profile of the [O I] λ5577 night-sky line for the wavelength coordinate. The deconvolved spectra have been reconvolved with an elliptical Gaussian with σ=0.625 Å in wavelength and σ=0.″24 along the slit.
Stockton *et al.* (see page 427)